PHYSICAL REVIEW C VOLUME 39, NUMBER 1 JANUARY 1989

Inelastic electron scattering from ^{13}C

D. J. Millener
Brookhaven National Laboratory, Upton, New York 11973

D. I. Sober, H. Crannell, J. T. O'Brien, and L. W. Fagg
The Catholic University of America, Washington, D.C. 20064

S. Kowalski and C. F. Williamson
Department of Physics and Bates Linear Accelerator Center, Massachusetts Institute of Technology, Cambridge, Massachusetts 02139

L. Lapikás
Nationaal Instituut voor Kernfysica en Hoge-Energiefysica, Amsterdam, The Netherlands
(Received 22 July 1988)

A detailed investigation of the excited states of ^{13}C below 10 MeV excitation energy by means of high-resolution electron scattering at momentum transfers between 0.4 and 2.4 fm^{-1} has been performed. Additional data taken for excitation energies between 10 and 22 MeV are also selectively discussed. Up to an excitation energy of 12 MeV the data are compared with the results of a shell-model calculation which uses the full $0\hbar\omega$ and $1\hbar\omega$ model spaces together with effective one-body transition operators.

I. INTRODUCTION

Inelastic scattering of medium energy electrons provides a well-understood probe of the charge, current, and magnetization densities which characterize nuclear excitations. In light nuclei, where the plane-wave Born approximation is quite accurate, provided a simple correction to the momentum transfer ($q \rightarrow q_{\rm eff}$) for Coulomb distortion is made, the connection between the measured form factors and the transition densities is direct and is simply expressed as a Bessel transform. Also, it is for light nuclei that the most extensive microscopic calculations of the transition densities can be performed and tested.

This paper reports on an extensive investigation of the excited states of ^{13}C using inelastically scattered electrons. The high q data were taken at the Bates Linear Accelerator with the high-resolution dispersion-matching system,[1] which made available significantly greater beam current, better resolution, and higher incident energy than were available in early work.[2–5] An additional improvement was made through the use of higher isotopic enrichment of the ^{13}C in the target. The data taken at Bates included form factors for momentum transfers between 0.5 and 2.4 fm^{-1}, with longitudinal-transverse separations for $q \geq 0.8$ fm^{-1}, for all states[6] below 10 MeV in excitation energy with the exception of the very broad $\frac{3}{2}^+$ state at 8.2 MeV. In addition, a number of excited states between 10 and 22 MeV have been investigated at three energies at a scattering angle of 90°, corresponding to 1 fm$^{-1} < q < 2$ fm^{-1}, for the purpose of comparison with other measurements[7,8] in this region at 180°. The low q data (0.4 fm$^{-1} < q < 0.9$ fm^{-1}) were taken using the 180° electron-scattering facility of the Instituut voor Kernphysisch Onderzoek (IKO).[9] In the figures which appear in this paper, data from the present work are identified by the acronyms Catholic University of America-Massachusetts Institute of Technology (CUA-MIT) or IKO, as appropriate.

The early work at Darmstadt[3] provides low q data (0.3 fm$^{-1} < q < 0.6$ fm^{-1}) for many levels. For a few levels, data (0.6 fm$^{-1} < q < 1.0$ fm^{-1}) were obtained at Saskatoon.[4] Measurements made at the Bates Linear Accelerator Laboratory by a University of Massachusetts group[7,8,10,11] of transverse form factors from 180° scattering have concentrated on the distribution of $M4$ strength[8] in ^{13}C and on a few selected states, for which the measurements have been extended to a high q of about 4.6 fm^{-1}. These latter states include the ground state,[10,11] the $\frac{1}{2}^+$ 3.09 MeV level[10] and the $\frac{9}{2}^+$ 9.50 MeV level.[10] Also, 180° measurements are available[7] for a number of other levels up to 22 MeV excitation energy.

Our experimental method is described in Sec. II, followed by a description of the data analysis in Sec. III. Before giving the experimental results, we present, in Sec. IV, an analysis of the relevant level structure of ^{13}C, together with an outline of our theoretical understanding of the structure of these levels. In the first instance, our theoretical treatment closely follows the approach of Lee and Kurath,[12,13] who perform shell-model calculations in $0\hbar\omega$ and $1\hbar\omega$ spaces for the negative- and positive-parity states, respectively. These calculations[14] use the Cohen-Kurath interaction[15] for the p-shell two-body matrix elements and the Millener-Kurath interaction[16] for all other (cross-shell) matrix elements. We begin Sec. IV by identifying those levels of ^{13}C which are predominantly of p-shell character. This leaves four negative-parity levels below 12 MeV, beginning with the 9.90 MeV $\frac{3}{2}^-$ level, which can be attributed to the excitation of two particles to the sd shell. The positive-parity levels in the same re-

gion appear to be of mainly $1\hbar\omega$ character, with those below 10 MeV having dominant components consisting of an *sd*-shell neutron coupled to the ground (0^+) and first excited (2^+) states of ^{12}C.

In Sec. V we present our experimental results for the form factors and compare them with the predictions of the shell-model calculations described in Sec. IV. Interwoven with the discussion of results is a discussion of the shortcomings of the limited model-space ($0\hbar\omega$ and $1\hbar\omega$) calculations and of the features of extended model-space [$(0+2)\hbar\omega$ and $(1+3)\hbar\omega$] calculations that are important for transitions of each multipolarity. As expected, longitudinal form factors are generally underestimated by the model. For "collective" transitions with surface-peaked transition densities, e.g., strong $C2$ and $C3$ excitations, a reasonable fit can be obtained by scaling the form factors (i.e., using effective charges). The transverse form factors, dominated in most cases by the magnetization current of the odd neutron, are overestimated typically by a factor of 2. Since the last neutron is relatively loosely bound, there are significant differences between transverse form factors calculated with harmonic oscillator wave functions and those calculated with more realistic Woods-Saxon wave functions. Further insight into the limitations of the model is obtained from an analysis of inelastic pion scattering[17] within the same framework.[13] In particular, the ratio[17--19] of π^+ to π^- cross sections provides information on the relative importance of neutron and proton excitations in a specific transition, and excitation functions at constant momentum transfer distinguish[20] between $\Delta S=0$ and $\Delta S=1$ transitions. Analyses of inelastic proton scattering on ^{13}C, using the same nuclear structure input, have also been performed for data taken at proton energies of 547 MeV (Ref. 21) and 135 MeV (Refs. 22 and 23), following an earlier analysis[24] of the 135 MeV data. The proton data provides further insights on the structure of ^{13}C, although the complexity of the *NN* interaction and its density dependence, particularly at the lower proton energy, make for larger uncertainties in the reaction mechanism.

We close in Sec. VI with a summary, further discussion, and conclusions.

II. EXPERIMENTAL METHOD

The high q data were taken using the high-resolution energy-loss magnetic spectrometer[1] at the Bates Linear Accelerator. Measurements were performed at fixed angles of 45°, 90°, and 160°, with the incident electron energy varied over the range from 78 to 339 MeV. The momentum transfer varied between 0.5 and 2.4 fm^{-1} (100 and 500 MeV/c). The energies of the 160° runs were selected to match the momentum transfer of the 90° (or 45°) runs. In all, spectra were taken at 33 different combinations of energy and angle during nine different running periods.

For most of the runs, data were taken only for excitation energies below 10 MeV. Because the detector spans a useful momentum range of 4%, one, two, or sometimes three different magnetic field settings of the spectrometer were required to span this excitation range, depending on the incident energy. In three additional runs at 90°, we explored the excitation region up to 22 MeV at incident energies chosen to match the momentum transfer of the University of Massachusetts (U Mass) 180° electron-scattering data.[8]

The target consisted of 25.6 mg/cm^2 of enriched ^{13}C powder contained between two 4.4 mg/cm^2 beryllium foils. In most cases, additional runs with a beryllium target were taken to facilitate separation of the beryllium background from the carbon data. The isotopic purity of the ^{13}C target was determined to be 97.46±0.05 % by comparison of the ^{12}C elastic and 4.44 MeV (2^+) impurity peaks from the ^{13}C target and from a calibration target of natural carbon. The ^{13}C target was determined to be uniform in thickness to within 2.5% over the beam interaction region by means of low-energy x-ray densitometry.

The energy resolution (FWHM) of the experiment varied from 48 keV in the lower-energy 90° runs to 80 keV in the higher-energy 160° runs, with a substantial fraction of the width due to energy-loss straggling in the target. This resolution is considerably better than that of previous electron-scattering investigations of ^{13}C, and facilitated the determination of excitation energies and widths of many excited states between 12 and 22 MeV. Some sample spectra are shown in Fig. 1.

The low q data were taken using the 180° electron-scattering facility of the IKO.[9] The target was a self-supporting foil of 73 mg/cm^2 thickness, enriched to 90% in ^{13}C. The data have been normalized to previous[25] IKO data on elastic 180° scattering from ^{13}C. Spectra up to 20 MeV excitation energy have been measured at $E_0=45$, 55, 70, 80, and 90 MeV (0.4 fm$^{-1}<q<0.9$ fm^{-1}) with an energy resolution of 350 keV.

III. DATA ANALYSIS

For the data taken at Bates, the incident energy and focal-plane parameters for each set of runs were determined from a least-squares fit to the well-known levels of ^{13}C and ^{9}Be with excitation energies below 10 MeV. The spectrum was then sorted into constant width energy bins (10, 15, or 20 keV) for subsequent analysis. Counting rate corrections for each spectrum were made based on coincidence scalers and other information recorded by the on-line computer.

The areas under all the peaks in the spectrum were calculated using an interactive fitting program derived from a code due to Bergstrom.[26] Each peak was described by eight parameters: height, position, Gaussian width, symmetric and asymmetric distortion terms, and radiative tail expressed as a Schwinger-type contribution plus two additional empirical terms. For peaks appreciably broader than the observed experimental resolution, a Breit-Wigner shape was used instead of the Gaussian form. In addition to the peak parameters, the fitting program included a four-term polynomial background contribution to approximate the radiative tails of off-scale peaks plus other slowly varying backgrounds. All parameters could be independently varied, singly or in groups, in order to minimize the χ^2 of the fit to the spectrum over a region of up to 250 data points (2.5 to 5 MeV of excitation energy range, depending on incident energy). For

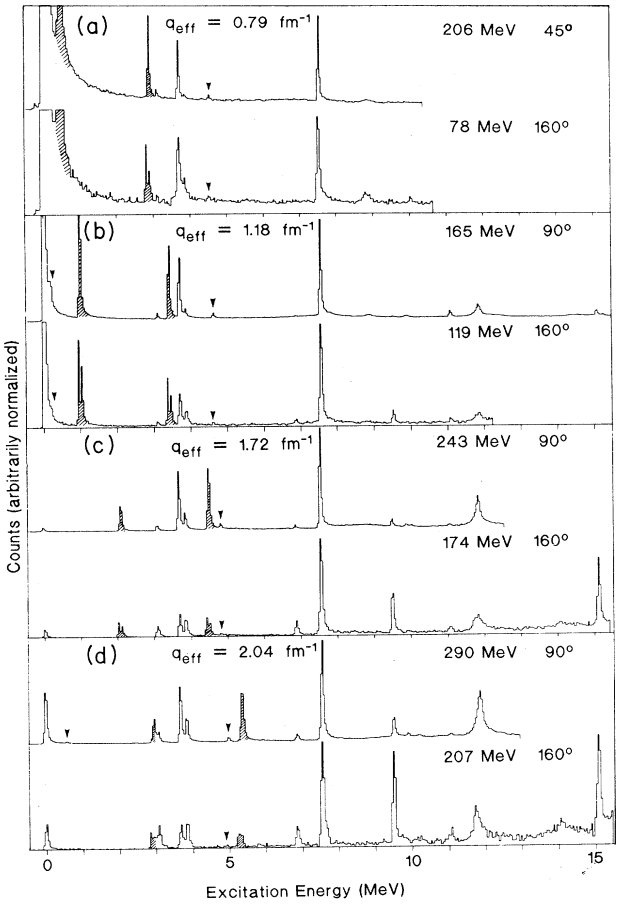

FIG. 1. Eight $^{13}C(e,e')^{13}C$ spectra are shown for four q matchings at the momentum transfers indicated in the part labels (a), (b), (c), and (d). The shaded areas correspond to excitation of the ^{9}Be ground and 2.43 MeV excited states. The arrows indicate the positions of peaks due to excitation of the ground and 4.44 MeV states of the ^{12}C impurity.

several well-separated peaks, the areas and statistical errors calculated by this procedure were compared with a direct summation procedure and found to agree, generally to within 1%. For each peak, the area was typically integrated from 1 MeV above to 0.5, 1.0, and 1.5 MeV below the peak maximum. These areas were then corrected for inner bremsstrahlung (Schwinger correction), external bremsstrahlung, and Coulomb straggling. The three integrated areas for each peak generally agreed to better than 1% after the radiative corrections were applied.

For the broader peaks, for which a Breit-Wigner shape was used, both the fitted width and the fitted area were corrected to account or the distortion of the experimentally observed line shapes by resolution effects. The correction factors were determined by fitting pseudospectra consisting of peaks constructed by the convolution of Breit-Wigner shapes with Gaussian resolution functions. An additional correction was made for counts lost in the tails of the Breit-Wigner distribution.

From the radiative-corrected areas, the cross sections and form factors were calculated using the measured values of integrated beam current, target thickness, and spectrometer solid angle. The efficiency of the focal-plane drift chambers was normally assumed to be 100%. The normalization of the cross sections was tested by comparing the ^{13}C and ^{12}C elastic scattering cross sections obtained from this experiment with those of previous measurements.[27,28] A few early sets of spectra showed inefficiencies of up to 15%, attributable principally to incorrect discriminator thresholds for the plastic Cherenkov counters which provide the event trigger. Peak areas in these spectra were corrected for this inefficiency. For the majority of spectra the elastic cross sections agreed well with previous values, and no correction was necessary.

Form factors are defined by the relationship

$$\frac{d\sigma}{d\Omega}(\theta)=\left[\frac{Z\alpha\cos(\theta/2)}{2E_0\sin^2(\theta/2)}\right]^2\frac{F^2(q,\theta)}{1+(2E_0/M)\sin^2(\theta/2)}\ , \tag{1}$$

where θ is the scattering angle, Z the nuclear charge, α the fine structure constant, E_0 the incident electron energy, M the nuclear mass, and q the three-momentum transfer. For those values of momentum transfer where data were available at two angles, longitudinal and transverse form factors were extracted according to the relationship

$$F^2(q,\theta)=\left[\frac{\Delta^2}{q^2}\right]^2\left[F_L^2(q)+\left[\frac{q^2}{2\Delta^2}+\tan^2(\theta/2)\right]F_T^2(q)\right]\ , \tag{2}$$

where

$$\Delta^2=4E_0E'\sin^2(\theta/2)$$

is the four-momentum transfer squared. For the kinematics of the present experiment, Δ^2/q^2 is always greater than 0.996.

To correct in lowest order for Coulomb distortion, the form factors were evaluated at the value of the effective momentum transfer

$$q_{\rm eff}=q\left[1+\frac{3Z\alpha}{2R_0E_0}\right]\ , \tag{3}$$

where $R_0=\sqrt{5/3}R_{\rm rms}$ and $R_{\rm rms}=2.48$ fm is the rms charge radius.[29] The effective momentum transfers of the points at the two angles used for Rosenbluth separation were always equal to within 0.05 fm^{-1}. No interpolation in momentum transfer was performed unless such interpolation changed the form factor at one of the two angles by more than its error bar. In practice, this interpolation was necessary only for several form factors evaluated for the 9.50 MeV state.

For the low q data taken at IKO, the spectra were radiatively unfolded up to $E_x=16$ MeV and the ^{12}C contribution was subtracted. Cross sections for the excited states were obtained from the unfolded spectra by a fit procedure employing Gaussian peak shapes plus a parabolic background. Above 16 MeV subtraction of the giant res-

onancelike background introduces uncertainties which are too large to obtain reliable results. For the unresolved 3.68 and 3.85 MeV levels, cross sections are available at more incident electron energies from the elastic-scattering experiment,[25] in which a 4 MeV excitation energy region was covered. Finally, we obtained transverse form factors by applying Eq. (1) and (2), where the longitudinal contribution F_L^2 could be neglected since at 180° it is weighted by a factor $(m_e/E_0)^2$ relative to the transverse form factor F_T^2.

IV. STRUCTURE OF ^{13}C BELOW 12 MeV

In Fig. 2 we have separated the low-lying energy levels of ^{13}C into groups classed as $0\hbar\omega$, $1\hbar\omega$, or $2\hbar\omega$. One of the least ambiguous ways of identifying the p-shell ($0\hbar\omega$) levels is through pickup reactions on p-shell targets. For example, the five levels identified as $0\hbar\omega$ below 12 MeV are all strongly excited in the ^{14}N(d,^{3}He)^{13}C reaction,[30,31] and the extracted spectroscopic factors[31] are in good agreement with the predictions of Cohen and Kurath.[32] All the $0\hbar\omega$ levels shown in Fig. 2 are populated in the ^{15}N(p,^{3}He)^{13}C reaction,[30] again in general agreement with theoretical expectations.[33] Finally, the ^{16}O(p,α)^{13}N reaction[34] picks out the analogs of the four members of the ^{13}C ground-state band (at 0, 3.68, 7.55, and 12.44 MeV), corresponding to the removal of three nucleons in a spatially symmetric state.[35] The relationship of the wave functions of these four states is evident from Table I, where the wave functions[15] of the $0\hbar\omega$ states are given in the SU3 version of LS coupling. We note that the $1/2_2^-$ and $3/2_2^-$ p^9 model states have large $S=\frac{3}{2}$ components. The predicted energies are in good accord with experiment except for the $3/2_2^-$ and $7/2_1^-$ levels which are predicted too low in energy. Fits[36] to an updated selection of p-shell energy level data (for $A=10$ to $A=16$) reproduce the ^{13}C $0\hbar\omega$ level scheme very well.

There are no candidates for the 9.90 MeV $\frac{3}{2}^-$, 10.75 MeV $\frac{7}{2}^-$, 10.82 MeV $\frac{5}{2}^-$, and 11.08 MeV $\frac{1}{2}^-$ levels in p-shell calculations. These levels should be predominantly $p^7(sd)^2$ in character in agreement with the calculations of Dubach.[37] The level ordering is characteristic of our expectations for $K=\frac{3}{2}$ and $K=\frac{1}{2}$ bands resulting from the coupling of two nucleons in lowest sd-shell Nilsson orbit to the ground state ($K=\frac{3}{2}$) and first excited ($K=\frac{1}{2}$) bands of an $A=11$ core. The relative prominence of the four "$2\hbar\omega$" levels in the ^{10}B(^{6}Li,^{3}He)^{13}C reaction[38] is consistent with the preceding interpretation. Experimental and theoretical studies of the appropriate two-nucleon

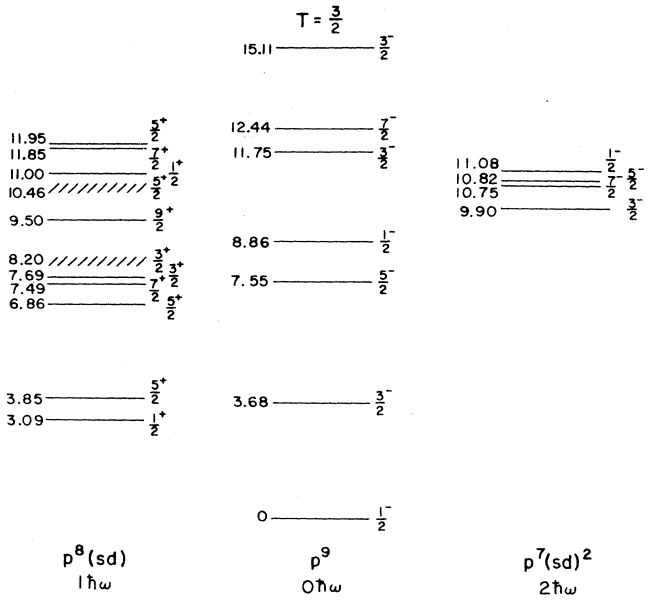

FIG. 2. Configurational identifications for the low-lying states of ^{13}C. The basis for the assignment of dominant configurations is given in the text.

TABLE I. p-shell wave functions[a] for ^{13}C.

	J^π		$\frac{1}{2}^-$	$\frac{3}{2}^-$	$\frac{5}{2}^-$	$\frac{1}{2}^-$	$\frac{3}{2}^-$	$\frac{7}{2}^-$	$\frac{3}{2}^-$
	T		$\frac{1}{2}$	$\frac{1}{2}$	$\frac{1}{2}$	$\frac{1}{2}$	$\frac{1}{2}$	$\frac{1}{2}$	$\frac{3}{2}$
	E_{exp} (MeV)		0	3.68	7.55	8.86	11.75	12.44	15.11
	E_{th} (MeV)		0	3.59	7.40	8.78	10.43	11.08	14.79
$(\lambda\mu)$[b]	L	S	Amplitudes						
(03)	1	$\frac{1}{2}$	0.840	0.937		0.154	−0.136		
(03)	3	$\frac{1}{2}$			0.913			0.961	
(11)	1	$\frac{1}{2}$	0.405	−0.037		−0.214	−0.377		0.845
(11)	1	$\frac{3}{2}$	−0.165	−0.270	−0.040	−0.750	−0.257		
(11)	2	$\frac{1}{2}$		0.217	0.301		0.361		−0.486
(11)	2	$\frac{3}{2}$	0.311	0.043	−0.272	−0.579	−0.802	−0.277	
(00)	0	$\frac{1}{2}$	0.076			0.180			
(00)	0	$\frac{3}{2}$							0.221

[a](8–16) potential interaction (Ref. 15).
[b]Spatial symmetry $[f]=[441]$ corresponds to SU3 symmetry (03), [432] to (11).

stripping reactions remain to be made.

The positive-parity levels in Fig. 2 below 12 MeV show a close correspondence to the predicted $1\hbar\omega$ spectrum, as can be seen in Table II. Here the theoretical spectrum has been normalized to the $\frac{5}{2}^+$ level at 3.85 MeV; this entails an upward shift[39] in the positive-parity spectrum by 0.5 MeV. The lowest eight states result primarily from the coupling of a neutron to the ground and first excited states of the ^{12}C core, in agreement with many earlier calculations, the first with a full $1\hbar\omega$ basis being that of Jäger *et al.*[40] Of these levels, the only one that could not be regarded as well established is the $5/2_3^+$ level, predicted at 10.23 MeV. However, Knox and Lane,[41] in an analysis of neutron-scattering data on ^{12}C, found a need to include a broad $\frac{5}{2}^+$ level, with a width of 1.23 MeV and with properties similar to the $5/2_3^+$ model state, in this region at 10.67 MeV. For all this group of states, SU3 symmetry (24) from the product $p^8[44]$ (04)$\times sd[1]$ (20) is dominant in the wave functions (column 4 of Table II and Fig. 3).

The remaining positive-parity states of direct interest for our analysis of inelastic scattering are the $7/2_2^+$ and $5/2_4^+$ levels. Lee and Kurath[13] predicted that these levels should be strongly populated by isoscalar $C3$ excitations in the inelastic scattering of electrons and pions (of course, the same is true for protons, alphas, etc.), and, indeed, they are.[17–20,22–24] A careful peak fitting analysis of the 135 MeV (p,p') data in the region $E_x \approx 11.8$ MeV by Collins[22,23] has identified states in this region at 11.75, 11.85, and 11.95 MeV and has made J^π assignments of $\frac{3}{2}^-$, $\frac{7}{2}^+$, and $\frac{5}{2}^+$, respectively. The strongest state in (p,p') is the 11.85 MeV level which exhibits a clear $C3$ angular distribution and is fitted extremely well in a distorted-wave calculation using a density-dependent nucleon-nucleon interaction[22,23] and the one-body density-matrix elements (OBDME) for the $7/2_2^+$ model state. Likewise, calculations for the $5/2_4^+$ level, which is predicted to be a factor of 2 weaker than the $7/2_2^+$ level, fit the angular distribution extracted for the 11.95 MeV level very well except at forward angles ($\theta < 20°$), where there may be contribution from nearby levels excited by transitions of lower multipolarity. The assignments given by Collins *et al.* are consistent[22,23] with analyses of data from other reactions and also with theoretical expectations. Thus, it would appear that the spin assignments for this region are now settled and that the tentative $\frac{3}{2}^-$ assignment for the 11.85 MeV level in the tabulation of Ajzenberg-Selove[6] should be changed to $\frac{7}{2}^+$.

We have noted in Table II that the $7/2_2^+$ and $5/2_4^+$ levels, together with the $1/2_2^+$ and $3/2_3^+$ levels, have the structure of a particle coupled to p^8 states of the $A=12$ core with [431] spatial symmetry, that is, the 12.7 MeV $(1^+;T=0)$, 15.11 $(1^+;T=1)$, 16.11 $(2^+;T=1)$, etc., levels. In more detail, the $5/2_4^+$ state is based 45% on core states with $T_c=0$, 55% with $T_c=1$, and is 80.7% $d_{5/2}$, 18.3% $d_{3/2}$, 1.0% $s_{1/2}$ particle. The corresponding percentages for the $7/2_2^+$ level are 38.5, 61.5, 63.1, 36.9, and 0.0. In an SU3 basis, the major components are from $p^8[431]$ (12)$\times sd[1]$ (20)$\rightarrow$[441] (32), with 74.9% (32) for $5/2_4^+$ and 69.0% (32) for $7/2_2^+$. Basically, the two states form a doublet with $L=3$ and $S=\frac{1}{2}$. For inelastic scattering, the dominant OBDME are those for $\Delta L=3$, $\Delta S=0$, $\Delta T=0$ (-0.468 for $5/2_4^+$, 0.572 for $7/2_2^+$), with the corresponding isovector OBDME an order of magnitude smaller, and the doublet forms the main source[13] of $C3$ strength in ^{13}C. Experimentally, the summed longitudinal form factors for the doublet contain about seven

TABLE II. Positive-parity wave functions[a] for ^{13}C.

J_n^π	E_{exp}	E_{th}	%(24)[b]	Wave function[c]
$1/2_1^+$	3.09	2.78	67.2	$0.945(0\times\frac{1}{2})+0.251(2\times\frac{5}{2})$
$5/2_1^+$	3.85	3.85[d]	73.8	$0.897(0\times\frac{5}{2})-0.357(2\times\frac{5}{2})$
$5/2_2^+$	6.86	7.25	85.2	$0.859(2\times\frac{1}{2})+0.485(2\times\frac{5}{2})$
$7/2_1^+$	7.49	7.57	82.3	$0.953(2\times\frac{5}{2})$
$3/2_1^+$	7.69	7.67	62.6	$0.932(2\times\frac{1}{2})+0.209(2\times\frac{5}{2})+0.109(0\times\frac{3}{2})$
$3/2_2^+$	8.2	7.86	76.8	$0.765(0\times\frac{3}{2})-0.522(2\times\frac{5}{2})-0.341(2\times\frac{3}{2})$
$9/2_1^+$	9.50	9.45	80.5	$0.955(2\times\frac{5}{2})$
$5/2_3^+$	10.46	10.23	56.6	$0.663(2\times\frac{5}{2})+0.501(2\times\frac{3}{2})-0.362(2\times\frac{1}{2})+0.211(0\times\frac{5}{2})$
$7/2_2^+$	11.85	12.46	69.0[e]	
$5/2_4^+$	11.95	12.11	74.9[e]	
$1/2_2^+$	(11.00)[f]	12.05	55.4[e]	
$3/2_3^+$	(12.11)[f]	12.93	55.9[e]	

[a]References 13 and 14.
[b]%(24) SU3 symmetry from the product $p^8(04)\times sd(20)$.
[c]Notation: $^{12}C(J)\times sd(j)$. Only large components are listed.
[d]Normalized.
[e]Based on levels of $A=12$ core with [431] spatial symmetry. The %(32) SU3 symmetry from the product $p^8(12)\times(sd)$ (20) is given. The weak-coupling strength is fragmented and is not given.
[f]Levels not studied in elastic scattering. No attempt has been made to verify these correspondences.

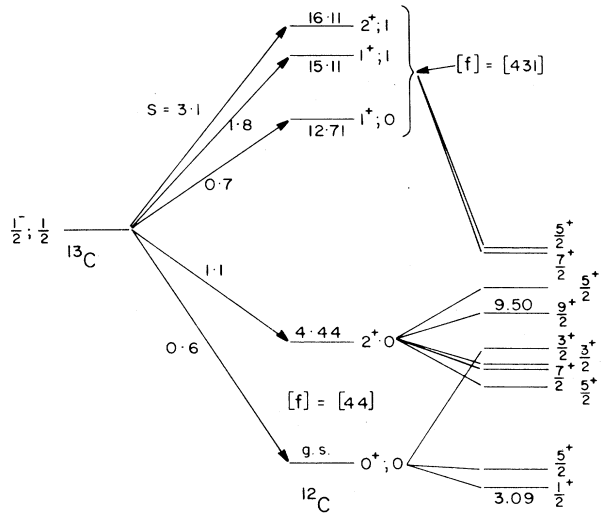

FIG. 3. Parentage of the ^{13}C ground state and of positive-parity states below 12 MeV excitation energy in ^{12}C. The pick-up spectroscopic factors (S) for the $T=\frac{1}{2}$ negative-parity states sum to 3 for $T=0$ core states and 6 for $T=1$ core states. Details of the parentage of positive-parity states are given in Table II.

times the strength of the 3.85 MeV $\frac{5}{2}^+$ level. It is interesting that the 3^- excitation built on the ^{13}C ground state is so unfragmented.

An outline of the parentage spectrum for the ^{13}C ground state and for the positive-parity states below 12 MeV excitation energy is given in Fig. 3, which summarizes much of the discussion in the preceding paragraphs. We note, particularly, that the $5/2_4^+$ and $7/2_2^+$ states based on core states with [431] spatial symmetry have the same overall spatial symmetry, [441], as the lowest positive states based on the ground and 4.44 MeV states of ^{12}C. The effective interaction favors high spatial symmetries and lowers these states considerably from where simple weak-coupling arguments would put them.

We give in Table III the OBDME for the states listed in Table II. The OBDME are given in LS coupling since the form factors are matrix elements of operators[42] which have $\Delta S=0$ character for the charge density or convection current and $\Delta S=1$ for the magnetization current. In fact, the OBDME are given in the SU3 coupling scheme since this introduces further simplicities into the interpretation of results. The relationship[43] between the SU3 OBDME and ordinary LS coupling is nontrivial only for $p\rightarrow sd$ and $\Delta L=1$, where a 2×2 transformation relates the $0p\rightarrow 1s$ and $0p-0d$ OBDME of Lee and Kurath[13] to SU3 OBDME with $(\lambda\mu)=(10)$ and (21) (or their conjugates); (10) corresponds to the orbital combination

$$\sqrt{1/6}(0p\rightarrow 1s)-\sqrt{5/6}(0p\rightarrow 0d)\ ,$$

and (21) to the orthogonal linear combination. Many of the OBDME in Table III do not contribute to electron scattering if harmonic oscillator wave functions are used. Specifically,

(i) the $\Delta J=0$ OBDME are included only for completeness;

(ii) for electric transitions with $\Delta S=1$ we have $\Delta L=\Delta J$;

(iii) for magnetic transitions with $\Delta S=1$ we have $\Delta L=\Delta J\pm1$.

Also, the effective interaction favors $(\lambda\mu)=(21)$ excitations over (10) excitations for low-lying levels. In fact, all (10) OBDME are small for the levels in Table III, but could be large for levels in the region of the giant dipole and the corresponding spin-flip resonances [at the photon point the $E1$ operator transforms as (10) $\Delta L=1\Delta S=0$ and the spin part of the $M2$ operator as (10) $\Delta L=1\Delta S=1$]. OBDME in the proton/neutron representation

$$(t_z|p\rangle=\tfrac{1}{2}|p\rangle)\ ,$$

are given by

$$Z_{p/n}=\frac{1}{\sqrt{2}}[Z_0\pm Z_1]\ , \tag{4}$$

where $Z_{\Delta T}$ is the matrix element of $a^\dagger\tilde{a}$ reduced in spin and isospin (OBDME of Table III) multiplied by the isospin Clebsch-Gordon coefficient $\langle T_iM_T\Delta T0|T_fM_T\rangle$. For $\Delta T=1$, the isospin Clebsch-Gordan coefficient for ^{13}C takes the values $-\sqrt{1/3}$ and $\sqrt{2/3}$ for $T_f=\frac{1}{2}$ and $T_f=\frac{3}{2}$, respectively. The dominance of (21) neutron excitations for the first eight states of Table II is evident in Table III. As remarked previously, the $7/2_2^+$, $5/2_4^+$ doublet is excited by $C3$ isoscalar excitations. The $1/2_2^+$ and $3/2_3^+$ states have large isoscalar matrix elements for the corresponding (21) $\Delta L=1$, $\Delta S=0$ excitation.

The harmonic oscillator shell-model form factors also display a simple behavior as a function of the SU3 quantum numbers. As is well known,[42] the form factors can be expressed in the form

$$F=y^{a/2}p(y)e^{-y}\ , \tag{5}$$

where $y=(bq/2)^2$, $p(y)$ is a polynomial in y, and $a=0$ or 1. For a pair of orbits with Q_1 and Q_2 quanta and fixed $(\lambda\mu)$, the maximum power of y in the longitudinal form factor is equal to $(Q_1+Q_2)/2$, and the minimum power is equal to $(\lambda+\mu)/2$. In the transverse form factor there is an extra power of $y^{1/2}$ if $\Delta S=1$ and of $y^{-1/2}$ if $\Delta S=0$. Also, the form of the polynomial depends only on $(\lambda\mu)$ and not on the multipolarity (a consequence of the Wigner-Eckart theorem applied to SU3); e.g., for $p\rightarrow sd$ transitions a factor $(1-\frac{1}{2}y)$ appears if $(\lambda\mu)=(10)$, and a factor y if $(\lambda\mu)=(21)$. Details of the form factors for pure SU3 excitations are given in Appendix A.

V. RESULTS AND INTERPRETATION

We present the experimental form factors, the extraction of which is described in Sec. III, for most levels in the form of figures which include the predictions of the model described in Sec. IV. In quoting our experimental form factors we have added a 5% systematic error in quadrature with the statistical errors of fitting. This systematic error was estimated by comparison of redundant measurements of many data points, and by observing the

fluctuations of the experimental form factors about smooth fitted curves. A complete tabulation of the measured form factors is given in Appendix B. Table VIII and Table X contain the form factors obtained from the CUA-MIT data for states below and above 10 MeV excitation energy, respectively. Table IX contains the ^{13}C excitation energies and widths determined in the same experiment. Table XI contains the form factors obtained from the IKO data. First, we give a brief description of the data obtained in this experiment for states up to 12 MeV excitation energy, including also the first $T=\frac{3}{2}$ state at 15.11 MeV. Comparisons with the data are then made for a variety of empirical and theoretical form factors.

A. Data for states below 12 MeV

Transitions to the $\frac{1}{2}^+$ 3.088 MeV, $\frac{3}{2}^-$, 3.684 MeV, and $\frac{5}{2}^+$ 3.854 MeV states appear clearly in all Bates spectra, e.g., Fig. 1, except where one state may be obscured by one of the ^9Be peaks. The $\frac{5}{2}^+$ state has not been resolved from its neighbor in earlier electron-scattering work, but

TABLE III. One-body density-matrix elements for positive-parity states in SU3 (LS) coupling.

			$0p-0s(10)$		$1s0d-0p(10)$		$1s0d-0p(21)$			
J_n^π	ΔJ	ΔT	$\Delta S=0$	$\Delta S=1$	$\Delta S=0$	$\Delta S=1$	$\Delta S=0$	$\Delta L=\Delta J-1$	$\Delta L=\Delta J$	$\Delta L=\Delta J+1$
$(1/2)_1^+$	0	0		−0.0501		−0.1363				−0.3618
		1		−0.0541		−0.2237				−0.6257
	1	0	−0.0784	0.0819	0.0392	0.1119	0.4924		0.4897	0.0683
		1	−0.0051	0.0578	0.1447	0.2721	0.6415		0.9101	0.0380
$(1/2)_2^+$	0	0		0.0175		−0.0710				−0.0439
		1		0.0019		−0.0865				−0.0374
	1	0	0.0293	−0.0066	−0.0146	−0.1299	0.7078		−0.1816	0.1869
		1	−0.0184	−0.0346	−0.0097	0.0231	0.1744		0.0165	0.0948
$(3/2)_1^+$	1	0	−0.0552	0.0329	0.0276	−0.1102	0.3498		−0.2266	0.0107
		1	0.0665	−0.0779	0.1055	−0.1568	0.6182		−0.3969	0.0014
	2	0		0.0004		−0.0017	−0.0236	−0.1060	0.0249	0.0735
		1		−0.0102		−0.0171	0.0402	−0.2399	0.0394	0.1403
$(3/2)_2^+$	1	0	0.0014	−0.0029	−0.0007	0.1416	0.0447		−0.0905	−0.3931
		1	−0.0028	0.0046	−0.0449	0.2144	0.0473		−0.1159	−0.6934
	2	0		−0.0006		−0.0106	−0.3357	−0.0000	0.1171	0.3242
		1		0.0007		−0.0600	−0.6354	−0.0076	0.1488	0.5808
$(3/2)_3^+$	1	0	−0.0513	0.0259	0.0257	0.1065	−0.5116		0.1418	−0.0006
		1	0.0617	−0.0618	0.2375	−0.0058	0.1074		−0.0857	0.1379
	2	0		0.0138		−0.1660	0.1275	−0.2229	−0.0563	−0.0848
		1		−0.0297		−0.1252	−0.0535	0.1936	−0.1800	−0.2330
$(5/2)_1^+$	2	0		−0.0009		0.1671	−0.2407	−0.1399	−0.3436	−0.0883
		1		−0.0016		0.2743	−0.4208	−0.2484	−0.6127	−0.1487
	3	0					0.4080	0.2858	0.2865	
		1					0.4596	0.6097	0.5610	
$(5/2)_2^+$	2	0		−0.0071		−0.0310	0.0953	−0.4057	0.0368	0.0265
		1		−0.0144		−0.0685	0.2017	−0.7343	0.0539	0.0538
	3	0					0.0390	−0.0798	0.0411	
		1					0.1425	−0.1383	0.0825	
$(5/2)_3^+$	2	0		0.0048		0.2581	0.1390	0.0750	−0.1780	0.0973
		1		0.0081		0.4418	0.3599	0.1212	−0.3046	0.1826
	3	0					0.4384	−0.0978	0.0169	
		1					0.4092	−0.0681	0.1572	
$(5/2)_4^+$	2	0		0.0029		0.0985	0.2433	−0.0187	−0.0084	0.1065
		1		0.0030		0.1328	0.2217	0.0334	−0.0658	0.1356
	3	0					−0.4675	0.2944	−0.0031	
		1					0.0479	−0.0203	−0.0144	
$(7/2)_1^+$	3	0					0.2753	−0.3907	0.0709	
		1					0.2919	−0.6035	0.1538	
	4	0							−0.1066	
		1							−0.2846	
$(7/2)_2^+$	3	0					0.5717	−0.1892	−0.1914	
		1					0.0667	0.2520	−0.2986	
	4	0							0.1851	
		1							0.1199	
$(9/2)_1^+$	4	0						0.4592		
		1						0.7670		

is easily distinguished here. In the IKO 180° data at low q, the $\frac{3}{2}^-$ and $\frac{5}{2}^+$ states are not resolved.

The transition to the $\frac{5}{2}^+$ state at 6.864 MeV is always weak in the 90° spectra, but becomes prominent in the 160° spectra, indicating the predominantly transverse nature of the transition.

The triplet of known $\frac{7}{2}^+$ 7.492 MeV, $\frac{5}{2}^-$ 7.547 MeV, and $\frac{3}{2}^+$ 7.677 MeV states is never directly resolvable, due primarily to the large size of the 7.547 MeV peak which dominates this region in all spectra. An attempt was made to determine peak areas for all three transitions by fixing their relative positions and widths. In nearly all cases, inclusion of the two smaller peaks improved the χ^2 of the fit in this region, but the evidence for their presence is not compelling, and the extracted form factors should be considered as upper limits rather than as reliable measurements. Data at 180° was obtained for the unresolved triplet of levels.

There was no visible evidence for the broad ($\sim$1 MeV) $\frac{3}{2}^+$ state at 8.2 MeV in the spectra and no attempt was made to fit this state. The relatively broad $\frac{1}{2}^-$ state at 8.86 MeV was seen clearly in the low momentum transfer spectra, including 180°, but was not clear at high q. Where the peak was not clearly seen, fits were obtained by fixing the known position and width of the peak.

The excitation of the $\frac{9}{2}^+$ 9.50 MeV state by inelastic electron scattering has been fully described by Hicks *et al.*[8] The present experiment has determined the energy of this level to be 9.500(7) MeV. Within experimental errors, this transition appears to be entirely transverse. The $\frac{3}{2}^-$ state at 9.897 MeV has a very small transverse form factor and was difficult to measure at 160°, although it appears clearly in the 90° data. Only upper limits on the form factor at low q could be obtained at 180°.

The states above 10 MeV were not studied systematically except in three 90° data runs at 165.7, 221.3, and 276.8 MeV incident electron energy, although states up to 12 MeV do appear in the spectra from several other runs. The $\frac{1}{2}^-$ 11.080 MeV state is clearly seen in all spectra which cover this excitation energy. The $\frac{7}{2}^-$ state at 10.753 MeV is not seen below a momentum transfer of about 1.5 fm^{-1}, but is seen at higher q, while the $\frac{5}{2}^-$ state at 10.818 MeV is seen at low q but disappears above 1.5 fm^{-1}. The state reported[6] at 10.996 MeV was not observed.

States at 11.748, 11.851, and 11.95 MeV are reported in the literature. Various combinations of these were tested in fits to the data in this region, but very consistent results were obtained using only a single level of energy 11.845(5) MeV and width 144(5) keV. This width is substantially greater than the 68(4) keV reported for the 11.851 MeV state. However, analysis[22,23] of the 135 MeV (p,p') data shows that the broader $\frac{5}{2}^+$ state at 11.95 MeV is populated only a factor of 2 less strongly than the 11.85 MeV state and we expect essentially the same ratio for longitudinal form factors. The (p,p') analysis used a width of 200 keV for the 11.85 MeV state compared with 500 keV from the tabulation. A state is observed at 11.80 MeV in the low q, 180° data, which we interpret as excitation of the $\frac{3}{2}^-$ 11.75 MeV state.

The narrow state at 15.106 MeV appears in all three 90° spectra, and provides an energy calibration point for all of the peaks in this region. Low q, 180° data was also obtained for this state.

B. Polynomial fits to form factors

The simplest form of empirical fit involves a polynomial fit in the variable $y=(bq/2)^2$ to quantities derived from the experimental form factors by dividing out the exponential and leading q dependences. This procedure is inspired by the traditional analysis of low q electron-scattering data and by the form of theoretical form factors when harmonic oscillator (HO) wave functions are used. We define (for $C0$ see the footnotes to Table IV)

$$B(C\lambda,q)=f^{-2}\frac{Z^2}{4\pi}\left[\frac{(2\lambda+1)!!}{q^\lambda}\right]^2 F_L^2 , \tag{6a}$$

$$B(E\lambda,q)=f^{-2}\frac{Z^2}{4\pi}\frac{\lambda}{\lambda+1}\frac{q^2}{k^2}\left[\frac{(2\lambda+1)!!}{q^\lambda}\right]^2 F_T^2 , \tag{6b}$$

$$B(M\lambda,q)=f^{-2}\frac{Z^2}{4\pi}\frac{\lambda}{\lambda+1}\left[\frac{(2\lambda+1)!!}{q^\lambda}\right]^2 F_T^2 , \tag{6c}$$

where $k=E_x/\hbar c$ and $f=f_{\rm SN}f_{\rm c.m.}e^{-y}$. The single-nucleon form factor, $f_{\rm SN}$, is taken from a four-pole fit by Simon[44] (parameters for G_E in Table III of Ref. 44 are used) although we could equally well have used a dipole form factor (see, e.g., Ref. 42), and $f_{\rm c.m.}=e^{y/13}$. Then, the fit is performed to

$$B(\lambda,q)^{1/2}=A+By+Cy^2+\cdots , \tag{7a}$$

$$=\left[\frac{b}{2}\right]^\lambda (A'+B'y+C'y^2+\cdots) , \tag{7b}$$

where b is the oscillator parameter. The number of terms in the polynomial is determined in part by consideration of the polynomial form expected on the basis of the shell-model structure with harmonic oscillator wave functions and in part by the requirement of a fit to the data. If F^2 exhibits a minimum then we provide a sign for F which differs on either side of the minimum and fit the quantity in Eq. (7).

To implement the fitting procedure described earlier, we have to make a choice for the oscillator parameter b which appears in the variable y. Clearly, the value of b and the number of terms included in Eq. (7) dictate the quality of the fit. We can also include b as a fitting parameter by setting $f=f_{\rm SN}$, in which case we fit to the expression in Eq. (7b) multiplied by $e^{12y/13}$. Details of polynomial fits for seven longitudinal form factors, for which only one multipole contributes, are given in Table IV. Since the protons in ^{13}C are quite deeply bound ($S_p=17.53$ MeV), the differences between form factors calculated with harmonic oscillator or Woods-Saxon wave functions are small, provided the rms charge radius of ^{13}C is reproduced in each case.

The lowest-order shell model corresponds to taking single term polynomials for $C2$ and $C3$ transitions and two terms for $C1$ transitions. Generally speaking, an ex-

cellent fit to the measured form factors is obtained by including one extra term beyond the lowest order in the polynomial, corresponding to an increase by two in the number of harmonic oscillator quanta involved in the transition. The same is true for the $C0$ transition, which vanishes in lowest order but requires two terms for a $\Delta\hbar\omega=2$ transition. Thus, the fitted values of the polynomial coefficients can be used to get some indication of the character and magnitude of the core polarization corrections needed to augment the shell-model transition densities. Of course, the fitted values depend on the number of coefficients and on the oscillator parameter. To provide a feeling for these sensitivities, several fits are listed for each transition.

Often, theoretical form factors are compared with data after the magnitude of the lowest-order shell-model result has been adjusted, e.g., by introducing effective charges. In many cases, a discrepancy in shape can be compensated for, to a large degree, by adjusting the value of the oscillator parameter. However, b values extracted from different transitions can vary considerably. We prefer to keep b near to the value required to give the measured rms charge radius or, equivalently, the elastic form factor up to the first minimum. The value of b obtained in this way for ^{13}C is 1.64 fm. We can then investigate whether there is a systematic correlation between shape discrepancies apparent for the lowest-order shell-model form factors and enhancement or quenching of the form factors by core polarization corrections. As a specific example, which we take up in more detail when we discuss the form factors for individual levels, consider the fits to the $C1$ transition to the 3.09 MeV level. With A, B, and C as parameters, χ^2 exhibits a minimum at $b=1.60$ fm. A good fit is also possible with b, A, and B as the parameters. However, in this case b, at 1.94 fm, turns out to be very much larger than we would expect based on the size

TABLE IV. Polynomial fits to form factors.[a]

Level/λ/N[b]	χ^2/DF	b	A	B		C
$(\frac{1}{2})^+$;3.09	0.385	1.70	0.1264(53)	0.1575(103)		−0.0306(39)
$C1$	0.335	1.64	0.1282(51)	0.1498(102)		−0.0358(40)
$N=19$	0.325	1.60	0.1295(51)	0.1439(103)		−0.0391(42)
	0.342	1.55	0.1311(50)	0.1355(104)		−0.0429(44)
	*0.347	1.601(97)	0.1295(60)		[3+b]	
	0.639	1.941(26)	0.1233(59)		[2+b]	
$(\frac{5}{2})^+$;3.85	0.447	1.53	6.250(131)	−0.071(63)		
$C3$	0.674	1.70	6.622(166)	−0.176(75)		
$N=13$	0.485	1.64	6.175(321)	−0.065(37)		−0.116(87)
	*0.491	1.527(65)	6.239(263)		[2+b]	
	0.683	1.725(11)	6.625(173)		[1+b]	
$(\frac{5}{2})^+$;6.86	0.612	1.64	1.766(228)	−0.108(120)		
$C3$	*0.608	1.704(68)	1.790(254)		[1+b]	
$N=14$						
$(\frac{3}{2})^-$;3.68	1.14	1.50	3.574(40)	−0.812(17)		
$C2$	1.21	1.64	3.543(86)	−0.061(100)		−0.107(23)
$N=15$	*1.24	1.505(23)	3.589(71)		[2+b]	
	5.49	1.797(13)	3.988(119)		[1+b]	
$(\frac{5}{2})^-$;7.55	0.726	1.50	4.437(36)	−1.049(21)		
$C2$	0.771	1.64	4.409(52)	−0.108(87)		−0.141(26)
$N17$	*0.771	1.495(20)	4.429(48)		[2+b]	
	3.96	1.776(113)	4.640(80)		[1+b]	
$(\frac{3}{2})^-$;9.90	1.86	1.40	0.506(22)	−0.117(13)		
$C2$	*1.61	1.64	0.451(42)	0.141(58)		−0.040(17)
$N=14$	1.97	1.344(95)	0.494(32)		[2+b]	
	2.33	1.629(25)	0.526(29)		[1+b]	
$(\frac{1}{2})^-$;8.86	1.55	1.64	0.687(12)	−0.243(10)		
$C0$	1.11	1.64	0.658(16)	−0.189(24)		−0.015(6)
$N=14$	*1.13	1.587(22)	0.659(15)		[2+b]	

[a]Equations (6) and (7) except $B(C0,q)=f^{-2}Z^2/4\pi(6/q^2)^2F_L^2$. Errors are given in parentheses for the fitted parameters. If the oscillator parameter is varied in the fit, the notation [$n+b$] indicates that an n term polynomial in Eq. (7) was used. An asterisk indicates the fit chosen to give the electromagnetic matrix elements listed in Table V.

[b]N is the number of data points.

of the nucleus. This behavior is typical of $C1$ transitions to low-lying states of light nuclei. Finally, with A, B, C, and D as parameters, D is undetermined and χ^2 remains flat at the minimum value as a function of b.

C. Electromagnetic transition strengths

The normal electromagnetic transition strengths, $B(E\lambda\uparrow)$ and $B(M\lambda\uparrow)$, are obtained from Eq. (7) for $q=k$. Essentially, $B(\lambda\uparrow)=A^2$, unless the transition is strongly hindered, in which case the contribution from the next power of q^2 may be significant. For the way in which we have defined the quantities in Eq. (6), the continuity equation ensures that the constant term in Eq. (7) has the same magnitude for $B(C\lambda)$ and $B(E\lambda)$.

In Table V we have collected together the available data on electromagnetic matrix elements which connect the ground state of ^{13}C to discrete excited states. The (e,e') results come from an analysis of the low-q data

TABLE V. Electromagnetic matrix elements $B(\lambda,\uparrow)$ W.u.

E_x (MeV)	J^π	λ	(e,e')[a]	(e,e')[b]	Other[c]	Theory[d]
3.09	$\frac{1}{2}^+$	$C1$	0.062(22)	0.047(5)	0.039(4)	0.024
3.68	$\frac{3}{2}^+$	$M1$	0.69(9)		0.79(7)	1.35
		$C2$	7.2(8)	7.1(3)	7.5(3.2)	8.1
3.85	$\frac{5}{2}^+$	$M2$			1.39(6)	1.50
		$C3$		3.9(3)	0.29(15)	3.9
6.86	$\frac{5}{2}^+$	$M2$	0.17(9)			0.11
		$C3$		0.32(9)		0.00
7.49	$\frac{7}{2}^+$	$C3$				2.5
		$M4$				13.7
7.55	$\frac{5}{2}^-$	$C2$	9.7(6)	10.8(3)	9.2(1.3)	10.7
		$M3$				0.16
7.69	$\frac{3}{2}^+$	$C1$			0.0071(12)	0.046
		$M2$				0.0029
8.2	$\frac{3}{2}^+$	$C1$			0.068(9)	0.0051
		$M2$				0.082
8.86	$\frac{1}{2}^-$	$C0$	0.59(5)	0.66(2)		
		$M1$	0.23(3)		0.37(4)	0.48
9.50	$\frac{9}{2}^+$	$M4$		77(3)		105
9.90	$\frac{3}{2}^-$	$M1$	0.033(5)			
		$C2$	0.091(30)	0.11(2)		
(10.46)	$\frac{5}{2}^+$	$M2$				4.41
		$C3$				5.18
11.08	$\frac{1}{2}^-$	$C0$	0.74(4)			
		$M1$	0.036(7)			
11.75	$\frac{3}{2}^-$	$M1$	0.20(5)			0.23
		$C2$				0.17
11.85	$\frac{7}{2}^+$	$M4$				0.79
		$C3$		27.5[e]		20.0
11.95	$\frac{5}{2}^+$	$C3$		e		11.2
		$M2$				0.19
15.11	$\frac{3}{2}^-$	$M1$	0.64(8)		0.63(4)	0.74
		$C2$	1.0(2)			0.54

[a]Reference 3.
[b]This work, from polynomial fits (see Table IV). For $C0$, $M=\sqrt{B(C0,k)}$ is given.
[c]Reference 14 for bound levels. Reference 61 for unbound levels.
[d]$0\hbar\omega$ and $1\hbar\omega$ calculations described in text. $b=1.64$ fm. For some of the unbound levels, most notably the 8.2 MeV level, the approximation of using harmonic oscillator wave functions will be poor.
[e]$B(C3\uparrow)=27.5$ W.u. is for the unresolved $\frac{7}{2}^+$, $\frac{5}{2}^+$ doublet. The number is given without error. Values obtained by using different empirical shapes for the $C3$ form factor (see the text) lie between 26.9 and 31.2.

from Darmstadt and from Table IV for the electric multipoles. The present analysis includes the Darmstadt data so that there should be agreement between the two sets of matrix elements up to small differences in the application of DWBA corrections to the data (choice of $q_{\rm eff}$ in our case). The only significant difference occurs for the $C1$ transition to the 3.09 MeV level. Here, it is clear from Fig. 4 of Ref. 3 that the fit to the matrix elements as a function of q^2 is not the best straight line through the data points. The best straight line would have a small positive slope in agreement with our result. The errors on our results in Tables IV and V are statistical and do not include an estimate for the model dependence in the fitting function. Some idea of the model dependence may be gained by looking at the variation in the leading term of the polynomial for different types of fits. The new results in Table V, for $B(C3)$ values, are, in principle, most subject to model dependence since low-q data is not available. Results for gamma transitions between bound states of ^{13}C are summarized in Ref. 14. There, for the $\frac{5}{2}^+$ 3.85 MeV level, the $B(C3)$ obtained from the mixing ratio[45] has large errors and disagrees with the value from the present analysis. The present value, despite the model dependence, provides a more reliable estimate of the $C3$ matrix element.

The theoretical values in Table V come from the $0\hbar\omega$ and $1\hbar\omega$ shell-model calculations described in Sec. IV. For $C2$ and $C3$ transitions effective charges have been used, the derivation of which is described in Sec. V D.

D. Effective charges

The present data can be used in conjunction with data on π^+/π^- cross-section ratios[17] to determine proton and neutron effective charges for $C2$ and $C3$ transitions. We write

$$\begin{aligned} A_p &= (1+\delta e_p)Z_p + \delta e_n Z_n \ , \\ A_n &= \delta e_n Z_p + (1+\delta e_p)Z_n \ , \end{aligned} \tag{8}$$

where

$$Z_{p/n} = 1/\sqrt{2}(Z_0 \pm Z_1)$$

are the shell-model OBDME in the p/n representation [see Eq. (4)]. For example, from Table III, the $\Delta L=3$, $\Delta S=0$ isoscalar OBDME Z_0 for the $\frac{5}{2}^+$ 3.85 MeV state and the $5/2_4^+$ and $7/2_2^+$ members of the 11.9 MeV doublet are 0.4080, -0.4675, and 0.5717, respectively, while the corresponding isovector OBDME Z_1 are -0.2653, -0.0277, and -0.0385. The weak-coupling character of the $5/2_1^+$ model state, exhibited in Table II, means that Z_n (0.476) will be considerably greater than Z_p (0.101). Without effective charges ($\delta e_p=\delta e_n=0$), F_L^2 is underestimated by a factor of about 9. We now use the $B(C3)$ to determine A_p through ($e_0=1+\delta e_p+\delta e_n$, $e_1=1+\delta e_p-\delta e_n$),

$$\begin{aligned} B(C3\uparrow) &= 60.964\frac{2J_f+1}{2J_i+1}(e_0Z_0+e_1Z_1)^2 e^2\mathrm{fm}^6 \ , \\ &= 12.146\frac{2J_f+1}{2J_i+1}A_p^2 \ \text{W.u.} \end{aligned} \tag{9}$$

The π^+/π^- cross-section ratio, given[17] as

$$R = \frac{\sigma(\pi^-)-\sigma(\pi^+)}{\sigma(\pi^-)+\sigma(\pi^+)} = 0.30(10) \ ,$$

together with $\sigma(\pi^-)\propto(3A_n+A_p)^2$ and $\sigma(\pi^+)\propto(3A_p+A_n)^2$, provides a quadratic equation for A_p/A_n in terms of R. We choose A_p/A_n to be positive since, for strong transitions, we expect the isoscalar matrix element to dominate. This analysis yields

$$1+\delta e_p = 1.20(33) \quad \text{and} \quad \delta e_n = 0.43(8)$$

or

$$e_0 = 1.63(34) \quad \text{and} \quad e_1 = 0.77(34) \ .$$

Taking these values for the effective charges, we obtain a prediction of $B(C3\uparrow)=31$ W.u. for the 11.9 MeV doublet. The range of experimental values given in Table V for this doublet was obtained by taking a shape for the $C3$ form factor from fits (Table IV) to the 3.85 MeV level and scaling it to obtain the best fit to the three data points for the form factor of the 11.9 MeV level. The ratio of F_L^2 for the doublet relative to the $5/2_1^+$ level is predicted to be 8.0 compared with about 7.2 for the observed ratio.

Overall, an isoscalar charge of $1.63e$ works very well for $C3$ transitions in light nuclei. For example, the $\frac{5}{2}^+$ ground state of ^{17}O means that $C3$ transitions occur to states with $J^\pi=\frac{1}{2}^-,\ldots,\frac{11}{2}^-$ and the effective charges deduced earlier give an excellent account of both (π,π') (Ref. 46) and (e,e') (Ref. 47) cross sections. In addition, (e,e') isovector transitions to $T=\frac{3}{2}$ states of ^{17}O are consistent with a quenching of about a factor of 2 for F_L^2. That δe_n is larger than δe_p is consistent with theoretical expectations (protons can excite core protons only through the $T=1$ two-body interaction). That $\delta e_0=\delta e_p+\delta e_n$ is positive and $\delta e_1=\delta e_p-\delta e_n$ is negative reflects the attractive (repulsive) nature of the $T=0$ ($T=1$) particle-hole interaction.

Exactly the same sort of analysis can be applied to the strong $C2$ transitions to the $\frac{3}{2}^-$ 3.68 MeV and $\frac{5}{2}^-$ 7.55 MeV levels. For the $\frac{5}{2}^-$ level, $e_0=1.61(6)$ and $e_1=0.68(6)$. The smallest uncertainties reflect the fact that the pion ratio[17] is more accurately known, $R=-0.26(3)$. With these effective charges, the $B(C2)$ predicted for the 3.68 MeV level is slightly larger than, but still in reasonable agreement with, the measured value. Again, the deduced effective charges are typical of those required in p- and sd-shell calculations.

E. Longitudinal form factors

Following the previous discussion of effective charges, which define effective one-body operators to be used for $C2$ and $C3$ transitions at low-momentum transfer, we now consider the description of longitudinal form factors over the full range of momentum transfers for which measurements have been made. Our prescription for using Woods-Saxon wave functions is described at the beginning of Sec. V F.

1. C2 transitions

The form factors for $C2$ transitions to $T=\frac{1}{2}$ states below 10 MeV excitation energy are shown in Fig. 4. The dotted curves correspond to the polynomial fits with $b=1.64$ fm from Table IV. The solid curves for the $\frac{3}{2}^-$ 3.68 MeV and $\frac{5}{2}^-$ 7.55 MeV members of the ^{13}C ground-state band are calculated using OBDME from the Cohen-Kurath potential interaction[15] together with the $C2$ effective charges obtained for the $\frac{5}{2}^-$ state in the previous section. The enhancement factors for the $\frac{5}{2}^-$ and $\frac{3}{2}^-$ levels are relatively small, being 1.57 and 2.16, respectively, at the photon point. This reflects that the fact that the $\Delta L=2$, $\Delta S=0$ proton OBDME are larger than the neutron OBDME for these levels, $Z_p/Z_n=0.692/0.157$ and 0.629/0.435, respectively.

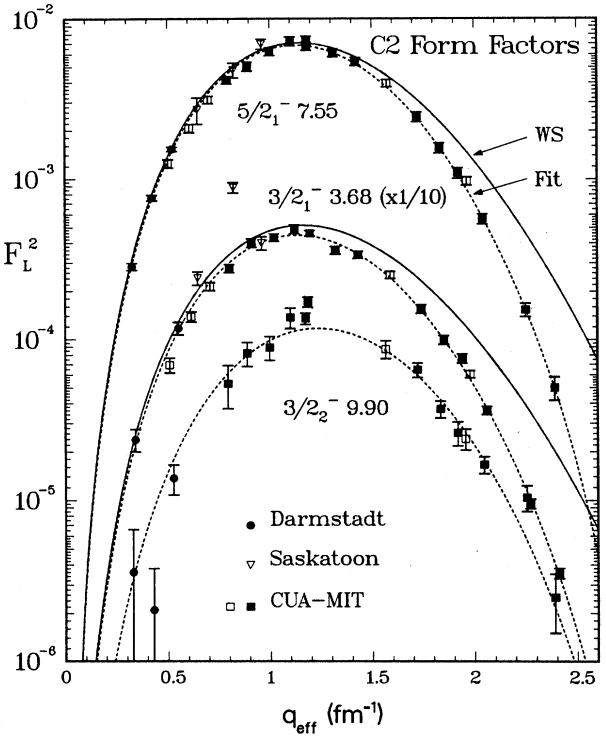

FIG. 4. $C2$ form factors for $T=\frac{1}{2}$ levels of ^{13}C. The labels for data from the present work in this and subsequent figures are squares for CUA-MIT data points and diamonds for IKO data points. For the CUA-MIT data points, solid squares mean that a Rosenbluth separation was made; open squares correspond to 45° or 90° form factors, for q less or greater than 1 fm^{-1}, respectively, with small transverse contributions, based on other data, subtracted. Circles are used to label Darmstadt data points (Ref. 3), triangles for Saskatoon data points (Ref. 4), and crosses for U Mass data points (Refs. 7–9). The error bars correspond to one standard deviation errors. When the one standard deviation error overlaps with zero, upper limits are given. The upper limits are obtained by adding two standard deviations to the value of the quantity. The dotted curves correspond to polynomial fits, described in Sec. V B, with $b=1.64$ fm, with the parameters taken from Table IV. The solid curves are the results of shell-model calculations which use Woods-Saxon wave functions and the effective charges discussed in Sec. V D. The various states are identified by their J_n^π and energy (in MeV).

The form factors are quite well reproduced up to the peak at $q\sim1.1$ fm^{-1}, but the theoretical form factors begin to deviate significantly from the data at larger momentum transfers. This point is demonstrated more clearly in Fig. 5 where the $C2$ matrix element is plotted, as a function of the variable $y=(bq/2)^2$, for the $\frac{5}{2}^-$ level. The harmonic oscillator prediction would be a horizontal line at $\sqrt{B(C2)}$ which, as expected, deviates little from the prediction with Woods-Saxon wave functions. If we expand the shell-model space to include $2\hbar\omega$ configurations, the negative-parity wave functions will be of the form

$$|\pi=-\rangle=\alpha|p^9\rangle+\beta|s^{-2}p^{11}\rangle+\gamma|p^7(sd)^2\rangle+\delta|p^8pf\rangle+\epsilon|s^{-1}p^9sd\rangle\ . \tag{10}$$

As is well known, small amplitudes of 1p-1h $1\hbar\omega$ configurations (δ and ϵ), corresponding to giant quadrupole excitations built on the initial or final states, are expected to provide the major source of enhancement to $C2$ matrix elements. The full polynomial parts of the form factors [Eq. (A1)] for pure SU3 transitions are

$$\begin{aligned}
&p\rightarrow p(\lambda\mu)=(11),\quad -\sqrt{8/15}y\ ,\\
&sd\rightarrow sd(\lambda\mu)=(11),\quad -\sqrt{40/15}y(1-2/5y)\ ,\\
&s\rightarrow sd(\lambda\mu)=(20),\quad \sqrt{4/15}y\ ,\\
&p\rightarrow pf(\lambda\mu)=(20),\quad \sqrt{20/15}y(1-2/5y)\ ,\\
&\mathrm{GQR}(\lambda\mu)=(20),\quad \sqrt{24/15}y(1-1/3y)\ ,
\end{aligned} \tag{11}$$

where the last line refers to the giant quadrupole resonance

$$(\sqrt{1/6}s\rightarrow sd+\sqrt{5/6}p\rightarrow pf)$$

built on a closed-shell ^{16}O ground state (small center-of-mass corrections have been neglected). Adding the requisite amount of GQR excitation to the basic $0\hbar\omega$ harmonic oscillator shell-model result to reproduce the observed $B(C2)$ leads to the dot-dashed line in Fig. 5, which improves the high-q behavior somewhat.

In Ref. 14, a $(0+2)\hbar\omega$ calculation which includes many, but not all, of the p^8pf and $s^{-1}p^9sd$ configurations is described. Total 1p-1h intensities of the order of 5% were obtained in this calculation, of which only a small part corresponds to $\Delta L=2$, $\Delta S=0$ proton excitations which enhance the $B(C2)$. As expected, the 1p-1h excitations in question turn out to be mainly isoscalar with a net destructive isovector contribution. The 1p-1h amplitudes need to be increased by a factor of a little more than 2 to obtain agreement with the observed $B(C2)$. However, the improvement in shape at high q is less than for the dotted line in Fig. 5. Complete $(0+2)\hbar\omega$ shell-model calculations have been performed[48] for p-shell nuclei. These calculations give wave functions 1p-1h admixtures of the order of 20% in intensity and require small effective charges ($\delta e_p,\delta e_n<0.1e$) to reproduce measured quadrupole moments. There are a number of consistency problems with such shell-model calculations.[49]

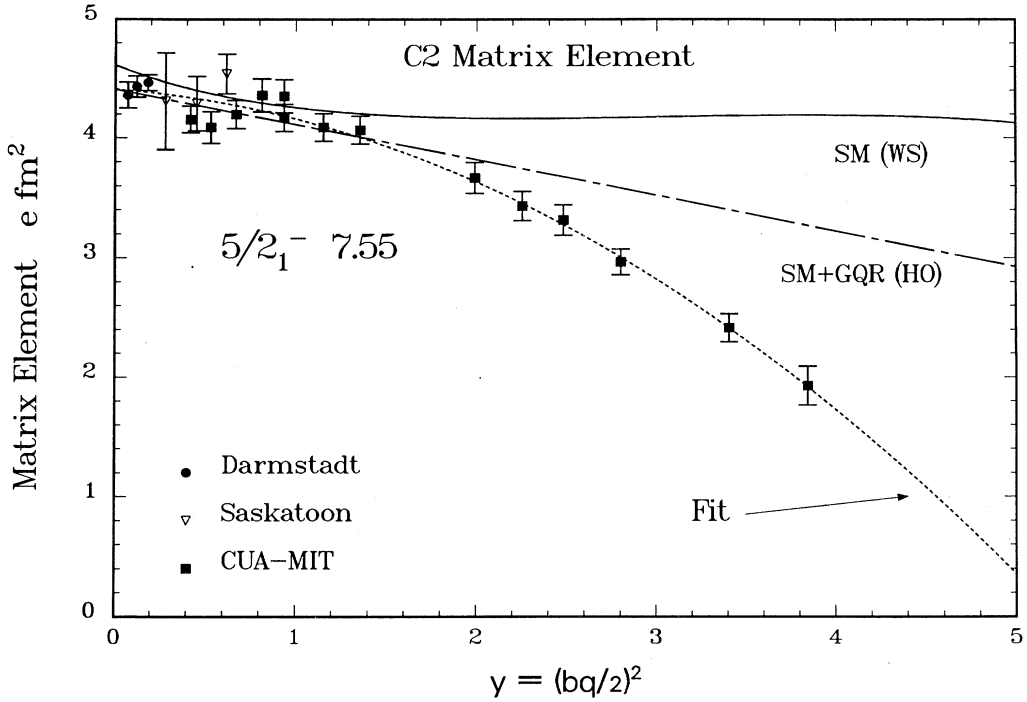

FIG. 5. The $C2$ matrix element, as defined in Eq. (6), for the $\frac{5}{2}^-$ 7.55 MeV level. The shell-model harmonic oscillator result would be a horizontal line at a value of 4.4 $e$fm^2. For the dot-dashed line, an amplitude of the giant quadrupole resonance, as defined in Eq. (11), sufficient to bring the unrenormalized shell-model $C2$ matrix element up to the experimental value, has been added.

For example, the matrix elements which admix the 1p-1h configurations involve large cancelling contributions from potential and kinetic energy terms. In any case, the observed q dependence cannot be obtained from a $(0+2)\hbar\omega$ calculation. Consequently, we would prefer to use an empirical one-body operator where the q dependence of the omitted configurations is carried in the single-particle matrix elements, or equivalently by the single-particle matrix elements of the density operator. We show in Fig. 6 the Woods-Saxon transition density for the $\frac{3}{2}^-$ 3.68 MeV state, calculated with bare charges, alongside the density derived from the fitted form factor. We note that the difference between the two densities shows a qualitative similarity to the transition density, arbitrarily normalized, for the GQR state. No error envelope has been obtained for the fitted transition densities. The behavior of the transition densities for the $\frac{5}{2}^-$ 7.55 MeV state is very similar. We could, therefore, use the difference density to define an effective one-body operator which would approximately reproduce the q dependence of the measured form factors. For a pure isovector transition, in which the form factor is reduced from the $0\hbar\omega$ shell-model value, the form factor would be expected to be enhanced relative to the peak at higher q values. Precise measurements are not available for pure isovector transitions. However, the reduction of the longitudinal form factor for the $\frac{3}{2}^-$; $T=\frac{3}{2}$ state at 15.11 MeV, shown in Fig. 7, is consistent with that expected from the square of the isovector effective charge derived in Sec. V D ($e_1^2=0.46$).

Finally, we notice from Fig. 4 that the form factor for the $\frac{3}{2}^-$ 9.90 MeV state is about a factor of 40 weaker than that of the $\frac{3}{2}^-$ 3.68 MeV level. From our discussion of the level scheme in Fig. 2, we concluded that the 9.90 MeV corresponded to the first member of a $K=\frac{3}{2}$ $p^7(sd)^2$ band. Indeed, a $(0+2)\hbar\omega$ calculation which includes the leading $2\hbar\omega$ configurations roughly reproduces the level ordering and suggested structure of the $2\hbar\omega$ states shown in Fig. 2. The reason for the particular weakness of the $C2$ transition to the 9.90 MeV can be traced to the fact that the dominant $p^7(sd)^2$ admixtures in the $K=\frac{1}{2}$ ground state will also have $K=\frac{1}{2}$. The transition strength should then be roughly proportional to the intensity of the relevant $p^7(sd)^2$ configuration and to the strength of a cross-band transition rather than an in-band transition.

2. *C0 transitions*

In the early low-q experiment at Darmstadt, monopole matrix elements were extracted for two excited $\frac{1}{2}^-$ levels at 8.86 and 11.08 MeV. As shown in Fig. 8, our new data define the $C0$ form factor for the $\frac{1}{2}^-$ 8.86 MeV level over the principal maximum and indicate the height of the expected second maximum. The $C0$ nature of the transition density for this state has been clearly evident in hadron, particularly proton,[21–24] scattering experiments. For the 11.08 MeV level there are three new data points from 90° measurements. Here, University of Massachusetts at Amherst (U Mass) measurements[7] at 180° have been used to subtract the transverse contribution of the $\frac{1}{2}^+$ 11.00 MeV, $\frac{1}{2}^-$ 11.08 MeV doublet for the two points at

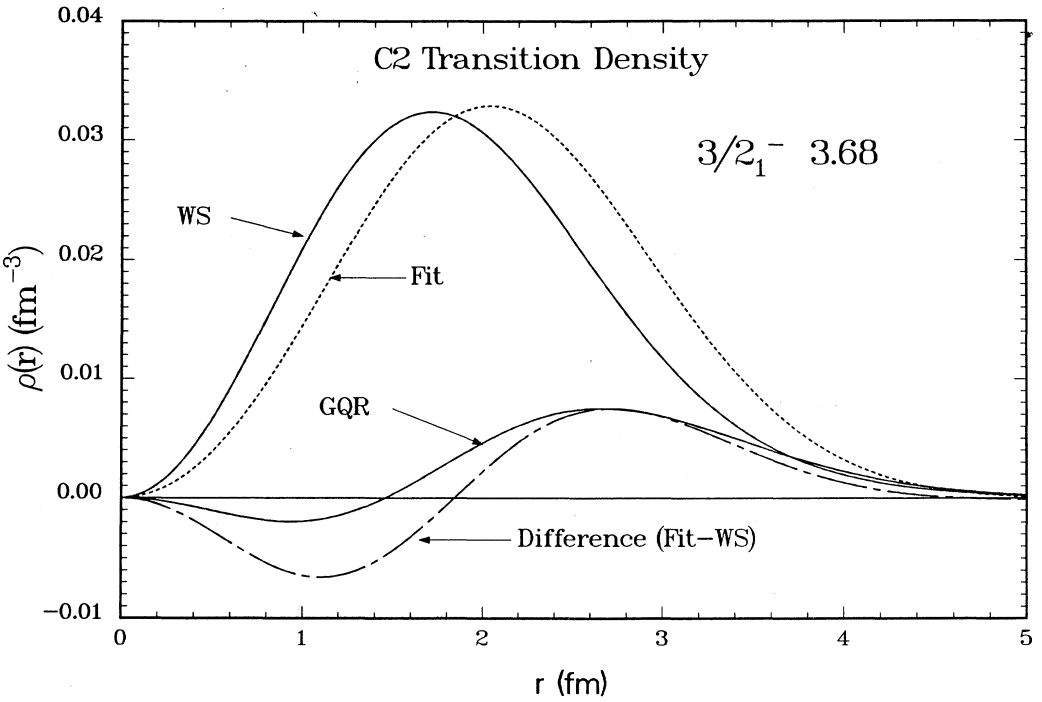

FIG. 6. Radial transition densities for the $C2$ transition to the $\frac{3}{2}^-$ 3.68 MeV level. The curve labeled GQR is for the specific combination of $s \rightarrow sd$ and $p \rightarrow pf$ excitations (arbitrarily normalized) discussed in the text.

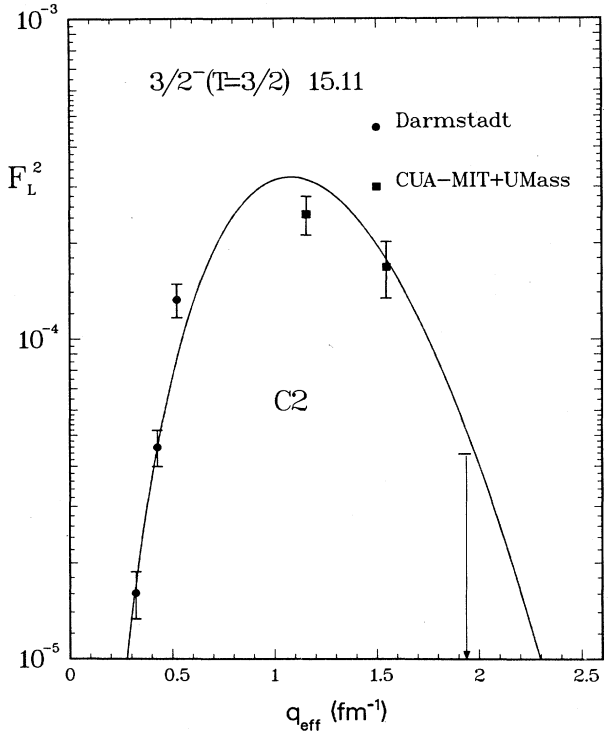

FIG. 7. $C2$ form factor for the $\frac{3}{2}^-$ $T=\frac{3}{2}$ level at 15.11 MeV. The high-q data points use CUA-MIT and U Mass data to perform a Rosenbluth separation.

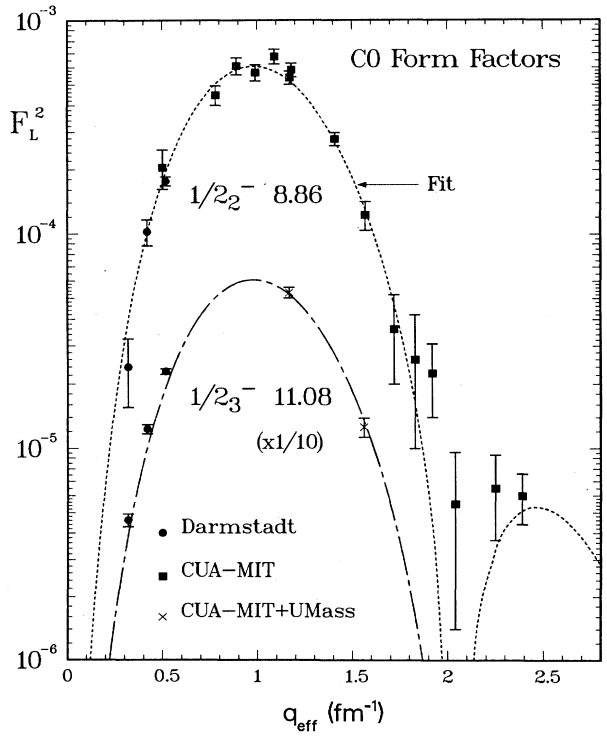

FIG. 8. $C0$ form factors for the $\frac{1}{2}^-$ levels at 8.86 and 11.08 MeV. For the 11.08 MeV level, U Mass data are used to subtract the transverse contribution.

highest momentum transfer. For the point near the peak of the form factor at $q=1.17$ fm^{-1}, the correction for the transverse component is expected to be very small: $F_T^2(M1)\simeq 5.4\times10^{-6}$ at $q=0.54$ fm^{-1} (Ref. 3), $F_T^2\sim 1.3\times10^{-5}$ at $q=1.59$ fm^{-1} (Ref. 7).

The $C0$ form factors shown in Fig. 8 are quite strong and are comparable in strength to the $0^+\rightarrow0^+$ transitions studied in such nuclei as ^{16}O (Ref. 50) and ^{18}O (Ref. 51). $C0$ transitions are never easy to describe theoretically since they depend sensitively on the radial makeup of the nuclear states.[52] At the lowest level, there is no $C0$ transition between the dominant p-shell components of the ground and 8.86 MeV states, and $2\hbar\omega$ admixtures in the states are required. The transitions can then be of two basic types. In the first, 1p-1h $2\hbar\omega$ admixtures of the giant monopole resonance play a role formally identical to that outlined for $C2$ transitions in the previous section. The pure SU3 polynomials are identical, up to an overall constant of $\sqrt{5/2}$, with those given in Eq. (11) [the GQR in Eq. (11) is replaced by a giant monopole resonance contribution]. The second type of transition takes place between the $p^7(sd)^2$ components in the initial and final states. The pure SU3 polynomials in this case (cf. Ref. 52) are

$$\begin{aligned} &p\rightarrow p(00),\quad \sqrt{3}(1-\tfrac{2}{3}y)\ ,\\ &sd\rightarrow sd(00),\quad \sqrt{6}(1-\tfrac{4}{3}y+\tfrac{1}{3}y^2)\ ,\\ &sd\rightarrow sd(22),\quad -\sqrt{\tfrac{2}{15}}y^2\ . \end{aligned}\tag{12}$$

The constant terms cancel out in a transition because of the orthogonality of the initial and final wave functions, and the resultant polynomial involves y and y^2 terms much as in the first case. The $C0$ transitions in the oxygen isotopes have been discussed within this framework by Horsfjord.[52] As for $C2$ transitions, the 1p-1h contributions can perhaps be included[52] in an effective one-body operator. The contributions from the 2p-2h admixtures have to be treated using an explicit model for the nuclear states. The two $(0+2)\hbar\omega$ calculations that we have performed, described in Ref. 14 and in the previous section, emphasize the two different types of components discussed above. A difficulty with the transition to the 8.86 MeV level, in particular, is that the initial and final p-shell wave functions have different intrinsic spins, $S=\frac{1}{2}$ and $S=\frac{3}{2}$ (Table I). Thus, the strong central part of the effective interaction, which conserves the intrinsic spin, does not admix configurations which contribute to $C0$ transitions. Of course, we do get a nonzero form factor, but much smaller than that observed. An explanation for the $C0$ form factor to the 8.86 MeV level thus presents an interesting puzzle. If our model for the $\frac{1}{2}^-$ 11.08 MeV level, basically $p^7(sd)^2$ with $K=\frac{1}{2}$, $L=1$, $S=\frac{1}{2}$, is correct, there is no mismatch of quantum numbers, and the $C0$ transition can proceed through the corresponding $p^7(sd)^2$ admixture in the ground state. Quantitatively, however, the calculated form factor is much too small.

The arguments above are based on the use of harmonic oscillator wave functions. Horsfjord[52] has demonstrated that considerable increases in $C0$ form factors can result when Woods-Saxon wave functions are used. At low q, for example, the fact that the rms radii of $1s$ and $0d$ orbits are no longer identical produces large changes (in effect, a cancellation is broken). The large difference in binding energies for the initial and final states could also lead to a p-shell contribution, although care must be taken[52] to eliminate terms which arise because the strict orthogonality of the initial and final states is broken by the prescription for using Woods-Saxon wave functions. More work on these rather delicate questions is necessary.

3. *C3 transitions*

The form factors for $C3$ transitions to the $5/2_1^+$ level at 3.85 MeV, the $5/2_2^+$ level at 6.86 MeV, and the unresolved $7/2_2^+$ and $5/2_4^+$ levels at 11.9 MeV are shown in Fig. 9. The relative magnitudes of the 3.85 and 11.9 MeV peaks are quite well reproduced by the shell-model calculations, which use the effective charges derived in Sec. V D, namely, $e_0=1.63$ and $e_1=0.77$. By using the strong isoscalar excitations at 11.9 MeV to define a slightly smaller isoscalar effective charge, one could then fit the 3.85 MeV peak, without impairing the agreement with the pion data, by slightly reducing the isovector effective charge. A cancellation between the isovector and isoscalar components, which are in any case small, for the transition to the $5/2_2^+$ 6.86 MeV level results in a very weak calculated form factor, which is not shown. We have a further remark to make about this transition when we discuss the transverse form factor in Sec. V F.

The shape discrepancy at high q, typical of longitudi-

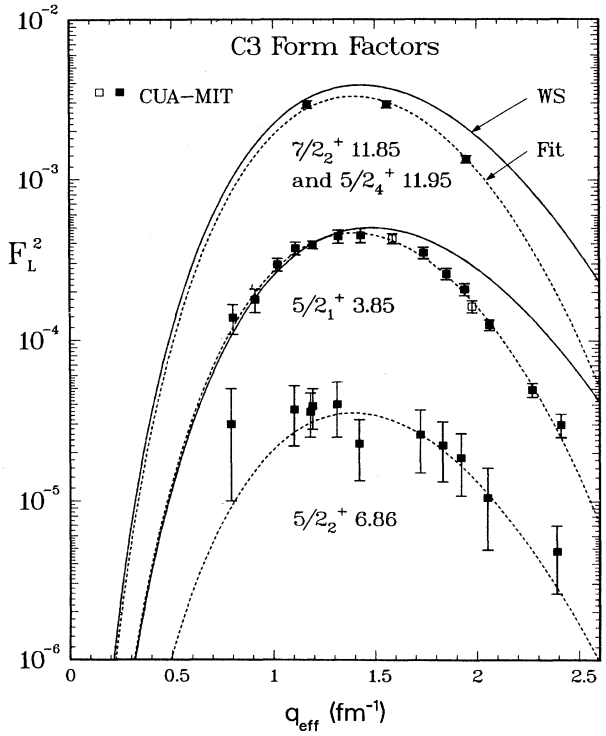

FIG. 9. $C3$ form factors for the $5/2_1^+$ 3.85 MeV, $5/2_2^+$ 6.86 MeV and unresolved $7/2_2^+$ 11.85 MeV and $5/2_4^+$ 11.95 MeV levels. See caption to Fig. 4.

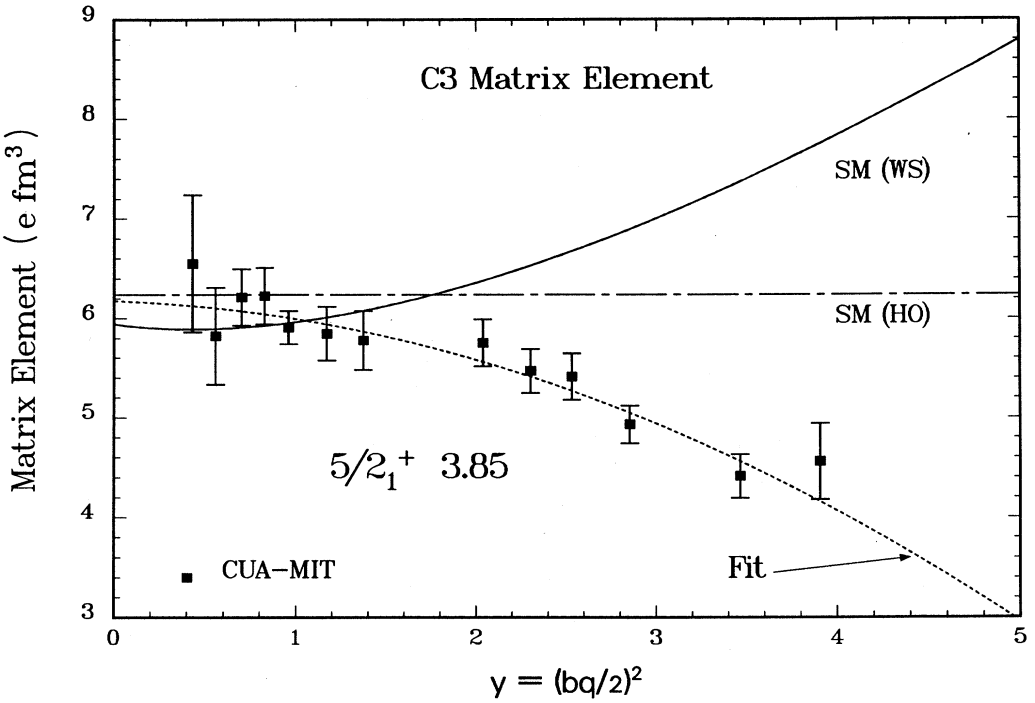

FIG. 10. $C3$ matrix element for the $\frac{5}{2}^+$ 3.85 MeV level. See caption to Fig. 5.

nal form factors, is again evident in Fig. 9, and is highlighted in Fig. 10, where the $C3$ matrix element for the transition to the 3.85 MeV level is given. The radial transition densities are shown in Fig. 11. The relationship between the fitted and shell-model transition densities is very similar to that for the $C2$ transitions, already discussed. The main difference is that, since the lowest $\frac{5}{2}^+$ level consists primarily of a neutron coupled to the two lowest states of the ^{12}C core, the basic $0\hbar\omega \rightarrow 1\hbar\omega$ $C3$ transition is weak, going by the small components of a

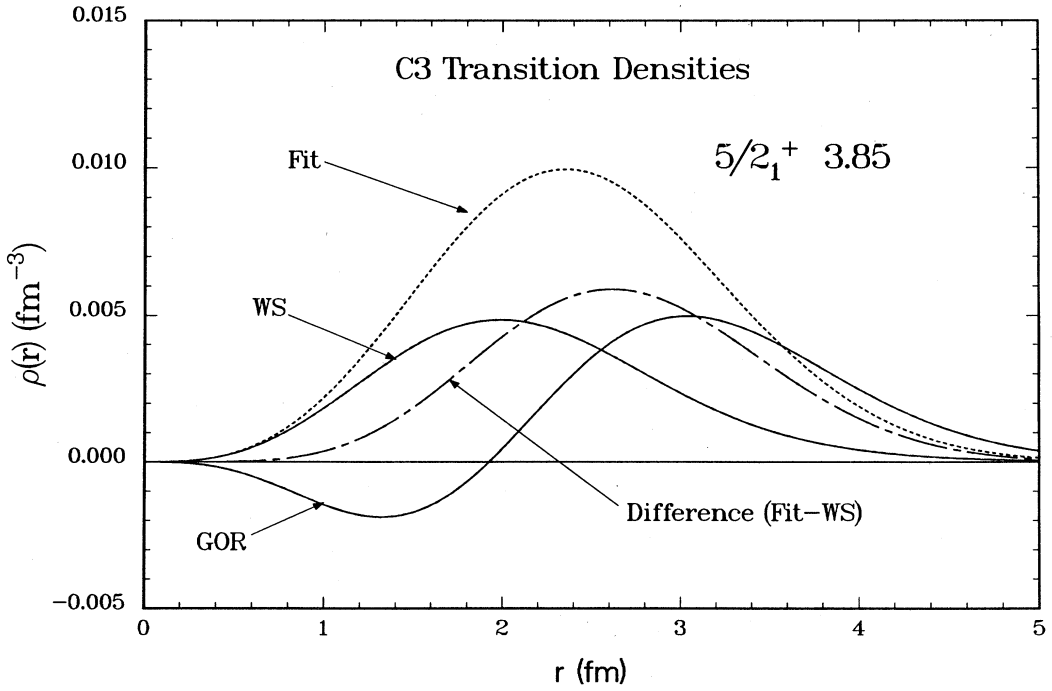

FIG. 11. Radial transition densities for the $\frac{5}{2}^+$ 3.85 MeV level. The curve labeled GOR is for the specific combination of $s \rightarrow pf$ and $p \rightarrow sdg$ excitations (arbitrarily normalized) discussed in the text.

proton coupled to $T=1$ states of the ^{12}B core.

Two important ways in which longitudinal form factors for non-normal parity states can be enhanced are through

(i) 2p-2h admixtures $[p^2 \rightarrow (sd)^2]$ in the ground state. A $p^8 d$ configuration can connect to both $0\hbar\omega$ p^9 and $2\hbar\omega$ $p^7 d^2$ configurations. For ^{13}C, this is a way to get protons involved in the transition. For example, the high-spatial symmetry configuration $(p^7[43]\times(sd)^2[2])$ [441] can be decomposed, symbolically, into

$$\tfrac{2}{3}\,(^{11}\mathrm{B}\times np)+\tfrac{1}{3}\,(^{11}\mathrm{C}\times nn)\ ,$$

while, for the similar coupling of a spatially antisymmetric $(sd)^2$ pair, the intensities are $\frac{2}{5}$ and $\frac{3}{5}$. Generally, the $p\rightarrow sd$ and $sd\rightarrow p$ amplitudes add constructively for $\Delta T=0$, $\Delta S=0$ excitations and destructively otherwise.

(ii) $3\hbar\omega$ 1p-1h admixtures into the $1\hbar\omega$ shell-model states. For $C3$ transitions such components correspond to admixtures of the $3\hbar\omega$ giant octupole resonance (GOR) built on the ground state. In the p shell, the $3\hbar\omega$ transitions arise from $s\rightarrow pf$ and $p\rightarrow sdg$ excitations, the pure SU3 polynomials being

$$\begin{aligned}
&p\rightarrow sd\,(\lambda\mu)=(21),\quad -\sqrt{8/35}\,y^{3/2}\ ,\\
&s\rightarrow pf\,(\lambda\mu)=(30),\quad \sqrt{8/105}\,y^{3/2}\ ,\\
&p\rightarrow sdg\,(\lambda\mu)=(30),\quad \sqrt{16/35}\,y^{3/2}(1-1/3,y)\ ,\\
&\mathrm{GOR}\ (\lambda\mu)=(30),\quad \sqrt{8/15}\,y^{3/2}(1-2/7y)\ .
\end{aligned}\tag{13}$$

For excitations of the ^{16}O closed-shell nucleus, the total $C3$ strength from the $s\rightarrow pf$ and $p\rightarrow sdg$ excitations (in the ratio 1:6) is $\frac{7}{3}$ that from $p\rightarrow sd$, if small center-of-mass corrections are ignored. Consequently, small $3\hbar\omega$ admixtures can be very effective in increasing the $B(C3)$ strength. It is apparent from Fig. 10, and the polynomial fits described in Sec. V, that a reasonable χ^2 fit to the matrix element could be obtained for a linear dependence on y. A rough calculation shows that a proton GOR OBDME of about 0.05 gives the slope observed in Fig. 10. For comparison, the shell-model proton $p\rightarrow sd$ OBDME has the value 0.10 (from the small components with $T=1$ core states). An $sd\rightarrow p$ (12) proton OBDME of about 0.15 would complete the fit. Equivalently, but not so obviously, it can be seen from Fig. 11 that enhancing the shell-model density through ground-state correlations, and then subtracting from the fitted density, would give a node in the difference density and improve the qualitative agreement with the GOR density.

4. *C1 transitions*

The $C1$ form factor for the $\frac{1}{2}^+$ 3.09 MeV level, in Fig. 12, and the corresponding matrix element in Fig. 13, show dramatically the failure, in both shape and magnitude, of the simple shell model to account for the transition. In many ways the failure is similar to that for the $C3$ transition to the $\frac{5}{2}^+$ 3.85 MeV level. However, some interesting additional points, which apply generally, can be made for $C1$ transitions between low-lying levels.

In the $1\hbar\omega$ model there are very strong constraints on the shape of the $C1$ form factor, and, to make this clear,

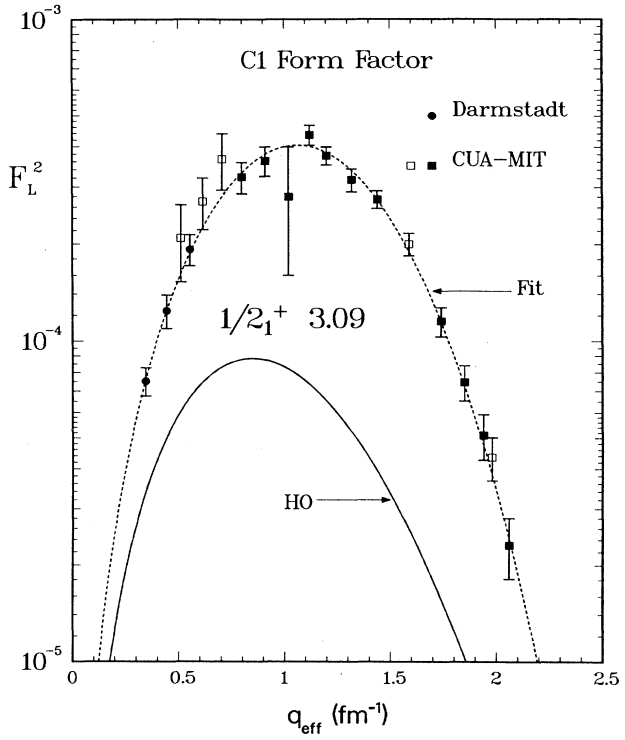

FIG. 12. $C1$ form factor for the $\frac{1}{2}^+$ 3.09 MeV level. See caption to Fig. 4.

it is convenient to use, once again, the SU3 basis. The relevant SU3 polynomials for the form factors are

$$\begin{aligned}
&p\rightarrow sd\,(\lambda\mu)=(10),\quad \sqrt{40/15}\,y^{1/2}(1-1/2y)\ ,\\
&p\rightarrow sd\,(\lambda\mu)=(21),\quad -\sqrt{2/15}\,y^{3/2}\ ,\\
&s\rightarrow pf\,(\lambda\mu)=(30),\quad \sqrt{4/15}\,y^{3/2}\ ,\\
&p\rightarrow sdg\,(\lambda\mu)=(30),\quad \sqrt{14/15}\,y^{3/2}(1-1/3y)\ .
\end{aligned}\tag{14}$$

The $p\rightarrow sd$ amplitudes for (10) and (21) are orthogonal linear combinations of $0p\rightarrow 1s$ and $0p\rightarrow 0d$ in the ratio $1{:}\sqrt{5}$ and *vice versa*. In an oscillator model the center of mass R and $E1$ operators transform as (10) under SU3 with $\Delta T=0$ and $\Delta T=1$, respectively. For nonspurious shell-model states, the matrix element of R is zero, and, for low-lying states, the $E1$ matrix element is approximately zero, so that the (10) OBDME are constrained to be small. The dominant (21) OBDME will then give a form factor with $C3$ shape. Actually, the ^{13}C transition under discussion is slightly pathological in that the $B(E1)$ is relatively large and that the state is mainly a neutron excitation, so that the (21) amplitude for $C1$ excitations is small. The transition densities are shown in Fig. 14(a) along with the pure (10) and (21) densities for comparison. The (10) density, appropriate for the giant dipole excitation, is surface peaked and gives rise to a large form factor peaked[43,49] at low q.

In all cases, the node in the fitted density occurs at a larger radius than for the (21) density. For ^{13}C, the difference between the fitted and shell-model densities, displayed in Fig. 14(b), shows a strong similarity to the

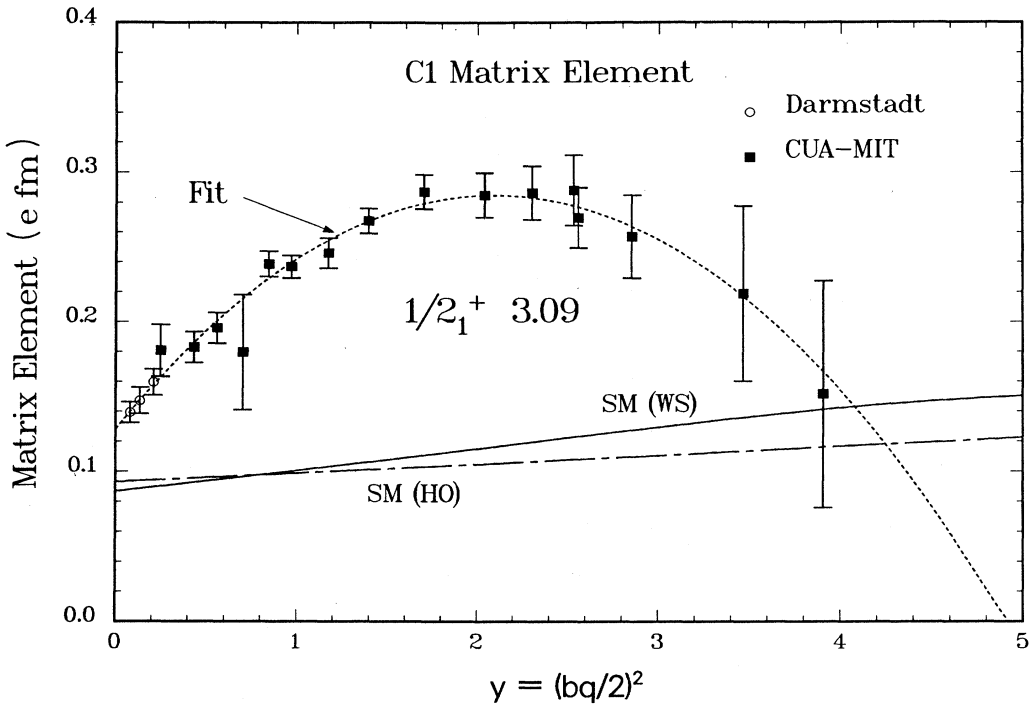

FIG. 13. $C1$ matrix element for the $\frac{1}{2}^+$ 3.09 MeV level. See caption to Fig. 5.

density for the combination of $3\hbar\omega$ single-particle transitions which maximizes the $y^{3/2}$ term in the polynomial. The HO shell-model gives for the matrix element

$$\sqrt{BC1(q)}=0.0930+0.0058y \ ,$$

while an excellent fit is obtained for

$$\sqrt{BC1(q)}=0.1282+0.1498y-0.0358y^2 \ .$$

For $C1$ transitions the admixed $3\hbar\omega$ terms do not affect the electromagnetic transition strength. From the listed polynomials, it can be seen that, if the (10) OBDME is constrained to be small, the total strength for the $C3$-like $y^{3/2}$ term from $s\rightarrow pf$ and $p\rightarrow sdg$ transitions is 14 times that for the basic $p\rightarrow sd$ (21) transition, so that these admixtures are particularly effective for $C1$ transitions.

The $1/2_2^+$ state, predicted at 12.05 MeV, provides an interesting contrast to the $1/2_1^+$ state. In Sec. IV, we noted that the $1/2_2^+$ and $3/2_3^+$ ($E_{\rm th}=12.93$ MeV) were related in structure to the $7/2_2^+$ and $5/2_4^+$ states of the 11.9 MeV doublet. The $\frac{1}{2}^+$ and $\frac{3}{2}^+$ states exhibit strong isoscalar $(\lambda\mu)=(21)$, $\Delta L=1$, $\Delta S=0$ OBDME equal to 0.708 and 0.512, respectively. The predicted longitudinal form factor for the $\frac{1}{2}^+$ level has a $C3$ shape with a peak value (no enhancements) of 1.4×10^{-4}. If we try to identify the $1/2_2^+$ level with the 10.996 MeV level,[6] we find that the predicted form factor is much larger than that observed for the 11.08 MeV peak at $q_{\rm eff}=1.95$ fm^{-1}.

F. Transverse form factors

The longitudinal form factors were not particularly sensitive to the choice of radial wave functions. From Table VI it can be seen that the use of Woods-Saxon rather than HO wave functions typically leads to reductions of the order of 5% in F_L^2. On the other hand, many of the transverse form factors are significantly reduced, a 50–60 % reduction being common for the $E1$ and $M2$ multipoles.

Our prescription for using Woods-Saxon wave functions is as follows. For a fixed diffuseness parameter (0.65 fm), the radius parameter of the Woods-Saxon wells for protons is chosen[49,53] to reproduce the rms charge radius[6,29] of ^{13}C. For neutrons, we assume that $\langle r_n^2\rangle\approx\langle r_p^2\rangle$, arguing that the np interaction tends to keep neutrons and protons together. Thus, we find $r_{\rm op}=1.41$ fm and $r_{\rm on}=1.25$ fm. A spin-orbit interaction is not included. To perform calculations with wave functions that are a function of the relative coordinate between particle and core $r_{i,c}$, the OBDME must be expressed in an appropriate form. Also, the contribution of each of the important core states to each of the OBDME has to be evaluated so that the particle separation energies are well defined. The well depth is then chosen to fit the separation energy in each case. The procedure is described more fully elsewhere.[49,53] The electromagnetic operators are functions of $r_i-R=(A-1)/Ar_{i,c}$, and the plane-wave Born approximation for (e,e') reactions can easily be adapted to this set of coordinates. Of course, no center-of-mass correction is required once relative coordinates are used. We feel most comfortable in applying this prescription to the low-lying positive-parity states since they possess a simple parentage spectrum to the ^{12}C core (Fig. 3). In this case, we might expect certain of the transverse form factors to exhibit characteristics of pure single-particle transitions, although this be-

havior may be masked when more than one multipole can contribute. Also, on account of the low binding energies, we can expect significant differences between the use of HO or Woods-Saxon wave functions. For states above the neutron threshold at 4.95 MeV, there can be a parentage to the ^{12}C ground state which then contributes to the particle width of the level; similarly, for states above 9.39 MeV with parentage to the ^{12}C 4.44 MeV level. For the ^{13}C transitions studied in this paper, contributions to transition densities from unbound neutron orbits are small compared to those from bound neutron orbits. For example, the largest OBDME contributing to the $\Delta J=2$

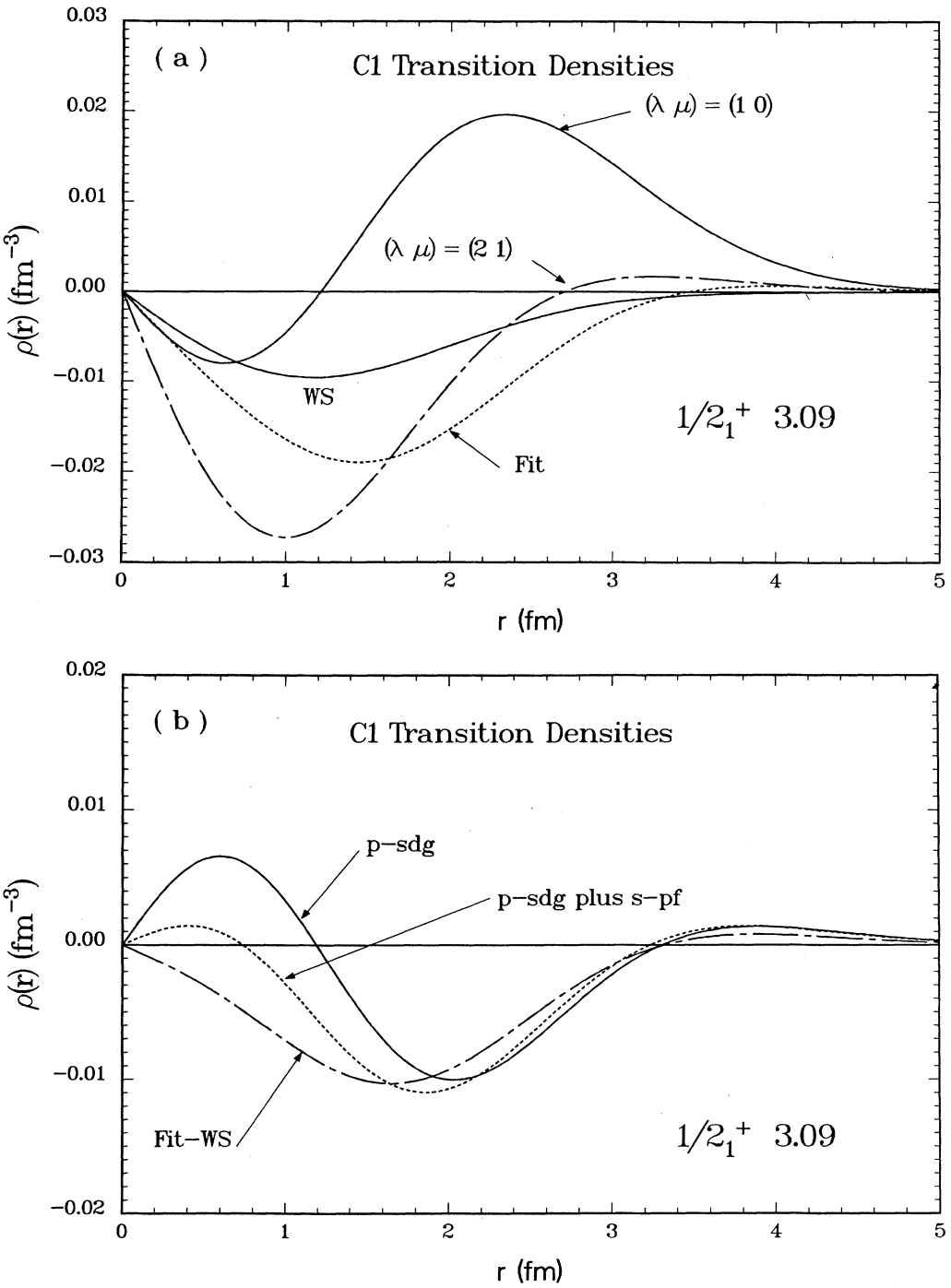

FIG. 14. (a) Radial transition densities for the $\frac{1}{2}^+$ 3.09 MeV level. Also shown are the densities for pure proton $p \rightarrow sd$ transitions with SU3 quantum numbers (10) and (21). (b) The difference between the density corresponding to the fitted form factor and the Woods-Saxon shell-model density is compared with densities for single-particle excitations through three shells (see the text). The $p \rightarrow sdg$ and $s \rightarrow pf$ densities correspond to SU3 (30) excitations and are arbitrarily normalized.

TABLE VI. Ratios of peak form factors calculated for ^{13}C with Woods-Saxon and harmonic oscillator wave functions.

J_n^π	E_x	Longitudinal		Transverse			
$\frac{1}{2}^-$	0	$C0$[a]		$M1$	0.78		
$\frac{1}{2}^+$	3.09	$C1$	0.95	$E1$	0.48		
$\frac{3}{2}^-$	3.68	$C2$	0.97	$M1$	0.64	$E2$	0.51
$\frac{5}{2}^+$	3.85	$C3$	0.97	$M2$	0.56	$E3$	0.74
$\frac{5}{2}^+$	6.86	$C3$	0.92	$M2$	0.60	$E3$	0.89
$\frac{7}{2}^+$	7.49	$C3$	0.95	$E3$	0.84	$M4$	0.82
$\frac{5}{2}^-$	7.55	$C2$	0.97	$E2$	0.79	$M3$	0.73
$\frac{3}{2}^+$	7.69	$C1$	1.04	$E1$	0.53	$M2$	0.31
$\frac{1}{2}^-$	8.86	b		$M1$	0.83		
$\frac{3}{2}^-$	11.75	$C2$	0.94	$M1$	0.73	$E2$	0.81
$\frac{3}{2}^-$	15.11	$C2$	0.89	$M1$	0.79	$E2$	0.79

[a]The HO and WS parameters are adjusted to reproduce the ground state $C0$ form factor.
[b]There is no $C0$ form factor with p-shell wave functions.

transition to the $5/2_2^+$ 6.86 MeV level is for a $0p_{3/2} \rightarrow 1s_{1/2}$ neutron transition with the ^{12}C 2_1^+ state as a core. This OBDME has a magnitude of 0.64, to be compared with -0.05 for the $0p_{1/2} \rightarrow 0d_{5/2}$ transition with the ^{12}C ground state as core. In such cases, we bind the orbit by a small amount and make little error in doing so. For the p-shell levels, the net OBDME for the pair of orbits $j_1 j_2$ may be small as the result of cancellations between contributions from widely spaced core states (Fig. 3). Thus, our prescription for handling the radial wave functions can give a significant contribution to a transition density even if the conventional OBDME, with the sum over all intermediate core states performed, is zero. This happens because different contributions are evaluated for different binding energies. A more sophisticated treatment of single-particle overlap functions[54] is perhaps called for.

In contrast to our multipole by multipole discussion of the longitudinal form factors in Sec. IV E, we consider the transverse form factors on a level by level basis. The contribution of two multipoles in most cases, and the possible interference between convection and magnetization current contributions, leads to a much greater variety of form factor behavior and motivates the case by case treatment. For the same reasons, and because of the inapplicability of harmonic oscillator wave functions, polynomial fits to the transverse form factors are limited in their usefulness. In connection with the contributions from the convection current, we note that the continuity equation is, in general, not satisfied when the one-body operators of the impulse approximation are used with shell-model wave functions. We follow the approach used by Heisenberg and coworkers in the analysis[55] of data and eliminate the convention current density $\rho_{\lambda,\lambda-1}(r)$ in favor of $\rho_{\lambda,\lambda+1}(r)$ and the transition charge density $\rho_\lambda(r)$. Thus,

$$F_\lambda^E(q) = -\left[\frac{\lambda+1}{\lambda}\right]^{1/2} \frac{\omega}{q} F_\lambda^C(q) - \left[\frac{2\lambda+1}{\lambda}\right]^{1/2} F_{\lambda,\lambda+1}^E(q) , \tag{15}$$

where $\omega = E_f - E_i$. $F_{\lambda,\lambda+1}^E(q)$ is evaluated directly from the shell-model OBDME while $F_\lambda^C(q)$ is scaled according to the effective charges derived in Sec. IV D to obtain a reasonable fit to the longitudinal form factor. Except at low q, or in special circumstances, the magnetization current of the odd nucleon usually dominates in ^{13}C.

1. The $\frac{1}{2}^+$ 3.09 MeV level

In Fig. 15(a) the pure neutron $0p_{1/2} \rightarrow 1s_{1/2}$ contributions to the form factor are compared to the data for both HO and Woods-Saxon wave functions. The $0p_{3/2} \rightarrow 0d_{5/2}$ contribution, shown only for Woods-Saxon wave functions, interferes destructively with the dominant $p \rightarrow s$ contribution at the first maximum, and moves the minimum to lower q. A large difference between the HO and Woods-Saxon cases is evident. If the neutrons were bound more deeply in the Woods-Saxon well so that the rms radii of the $0p_{1/2}$ and $1s_{1/2}$ orbits matched the HO values, one might have surmised that the $p \rightarrow s$ form factors could be made quite similar, but such is not the case. The result of adding in the contributions from protons, largely through $F_\lambda^C(q)$ in Eq. (15), and other pairs of orbits is shown in Fig. 15(b). The Woods-Saxon form factor now matches the data quite well out to $q_{\text{eff}} = 2$ fm^{-1}. The HO form factor is about twice as large and reproduces the position of the minimum less well. Neither calculation can reproduce the data (which extends[10] out to $q_{\text{eff}} = 4.25$ fm^{-1}) at high q, a problem which exists for a number of low multipolarity transverse form factors.[10] It is possible that whatever core polarization corrections are

necessary to reproduce the high-q behavior of the form factor will destroy the apparently good agreement that the Woods-Saxon calculation exhibits at low q.

2. *The $\frac{3}{2}^-$ 3.68 MeV and $\frac{5}{2}^+$ 3.85 MeV levels*

Although the present CUA-MIT data resolve the 3.86 and 3.85 MeV levels, the data does not extend to a low enough q to fully define the peak for the $M1$ form factor of the 3.68 MeV level. Consequently, we consider also the form factor for the unresolved doublet as defined by the present 180° IKO data, the Darmstadt data[3] at low q and the 180° U Mass data,[7] which has smaller statistical errors than the CUA-MIT data obtained from a Rosenbluth separation.

The CUA-MIT data for the $\frac{3}{2}^-$ 3.68 MeV and $\frac{5}{2}^+$ 3.85 MeV levels are shown in Fig. 16 and Fig. 17, respectively, while the combined data is shown in Fig. 18. Figure 18(a) illustrates the differences between HO and Woods-Saxon wave functions for the $M1$ and $M2$ form factors which are important at low q. Figure 18(b) compares the combined total of the Woods-Saxon $M1$, $E2$, $M2$, and $E3$ form factors with the data.

It is evident from Table V that the p-shell calculation overestimates the $M1$ matrix element by a considerable factor. A similar problem occurs for the related Gamow-Teller matrix element, deduced from the $^{13}C(p,n)^{13}N$ reaction at 160 MeV (Ref. 56) and 800 MeV (Ref. 57). Some quenching of the $M1$ matrix element is expected on the basis of calculations of second-order core polarization, isobar-current, and meson-exchange current processes performed by Towner and Khanna.[58] However, the effective g factors listed in Table VI of Ref. 58 give only a 10% quenching of the $B(M1)$ value for the $\frac{1}{2}^- \rightarrow \frac{3}{2}^-$ transition in ^{13}C. Since the origin of this discrepancy is not clear, we normalize our calculated $M1$ form factor to reproduce the experimental value at the photon point. All the squared $M1$ form factors in Figs. 16 and 18 are accordingly multiplied by a normalization factor of 0.53. From Fig. 18(a), it can be seen that the Woods-Saxon $M1$ form factor gives a better representation of the q dependence of the form factor for $q < 1$ fm^{-1} than does the HO $M1$ form factor. If the binding energies for the $p_{1/2} \rightarrow p_{3/2}$ contribution based on the ^{12}C ground-state core are increased, the Woods-Saxon form factor more closely resembles the HO form factor.

The $M2$ form factors in Fig. 18(a), both normalized to the experimental $B(M2)$ value, show a distinct difference in q dependence. In this case, the HO form factor is not renormalized, while the Woods-Saxon form factor squared is reduced by a factor of 0.59. The difference in $B(M2)$ values for the two cases is due to the larger radial extent of the Woods-Saxon wave function for the loosely bound neutron.

Figures 16, 17, and 18 show that the Woods-Saxon $M1$ and $M2$ form factors give a reasonable account of the low-momentum transfer data once they are normalized to reproduce the electromagnetic matrix elements. Clearly, however, it would be useful to have low-q 180° data which resolves the two states.

At higher q the $E2$ and $E3$ multipoles dominate. The

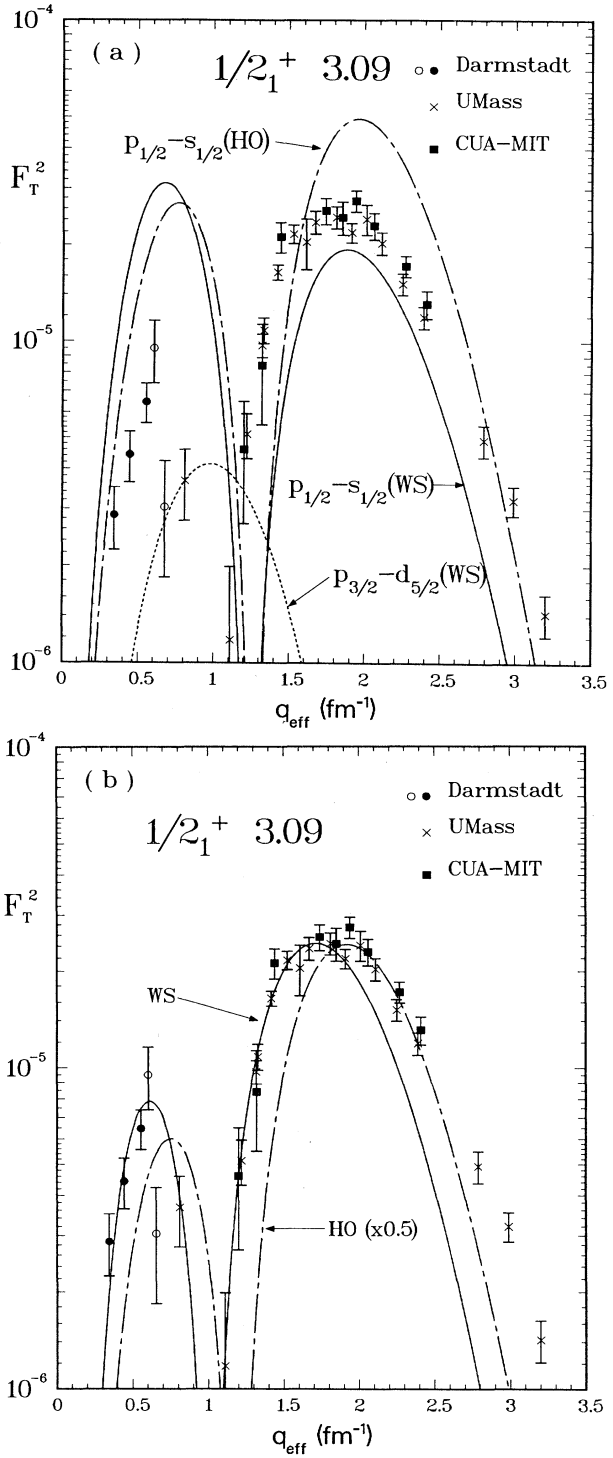

FIG. 15. (a) Pure neutron $0p_{1/2} \rightarrow 1s_{1/2}$ and $0p_{3/2} \rightarrow 0d_{5/2}$ transverse form factors, calculated with Woods-Saxon and harmonic oscillator radial wave functions, for the $\frac{1}{2}^+$ 3.09 MeV level. The strengths are determined by the shell-model one-body density matrix elements. The two amplitudes interfere destructively at low q. The open circle data points are obtained from Darmstadt measurements (Ref. 3) at 164.9° with the longitudinal contribution (Fig. 12) subtracted. (b) Form factors for the same transition, calculated from the full set of shell-model amplitudes.

$E3$ form factor in Fig. 17 is obtained by reducing the magnetization current contribution by a factor of 0.707. Essentially, this can be viewed as a renormalization of the isovector g factor analogous to the reduction of the isovector charge for $C2$ and $C3$ transitions. As a general rule, this renormalization is typical of that required for the magnetization current contributions to $E2$, $E3$, and $M4$ form factors. The $E2$ form factor for the 3.68 MeV level would require a similar renormalization if the $p_{1/2} \rightarrow p_{3/2}$ neutron contribution based on the ^{12}C g.s. was evaluated for deeply bound wave functions (cf. the ratio of Woods-Saxon to HO in Table VI). In more detail, a contribution to the OBDME from the ^{12}C g.s. core of $+0.41$ would be cancelled, for HO wave functions, by a contribution of -0.37 from core states above 12 MeV in excitation energy. The Woods-Saxon $E2$ form factor in Fig. 16 requires no renormalization to reproduce the data points for $q \sim 1.8$ fm^{-1}. Since we would, in any case, scale the magnetization current contribution to the simple p-shell form factor, the preceding discussion should be taken mainly as an indication that a more refined treatment of the radial dependence of single-particle wave functions is called for. Another noteworthy point concerning the $E2$ form factor is that there is destructive interference between convection and magnetization current contributions at low q. Even at the peak the interference reduces the form factor from the magnetization current alone by a factor of 2.

The overall comparison in Fig. 18(b) shows that the total form factor for the doublet agrees quite well with the data except for the dip near $q=1.1$ fm^{-1}. An improvement would occur if the minimum of the $M1$ form factor could be moved in to $q \sim 1$ fm^{-1} in the process of reducing the form factor at low q. Then it is likely that the second maximum of the $M1$ form factor would gain in strength necessitating a reduction in the $E2$ form factor, and thus the total form factor for $q \sim 1.1$ fm^{-1}. A precise measurement of the transverse form factor for the $\frac{3}{2}^-$ 3.68 MeV level, alone, would help greatly in deciding whether the above scenario is tenable.

3. *The $\frac{5}{2}^+$ 6.86 MeV level*

There are only two large OBDME involved in the excitation of the 6.86 MeV level. These are for $0p_{3/2} \rightarrow 1s_{1/2}$ (OBDME=0.63) and $0p_{3/2} \rightarrow 0d_{5/2}$ (OBDME=0.28) neutron transitions for $\Delta J=2$ based on a ^{12}C 4.44 MeV core. The Woods-Saxon form factors without any renormalization are shown in Fig. 19(a). The $M2$ contribution clearly dominates. From Table VI it can be seen that HO wave functions give a much larger $M2$ form factor. The $M2$ form factor exhibits a minimum, which is not apparent in the data, at $q=0.8$ fm^{-1}. The fact that the $M2$ form factor for the $5/2_2^+$ level has a maximum at low q suggests that a small admixture of the $5/2_1^+$ model wave

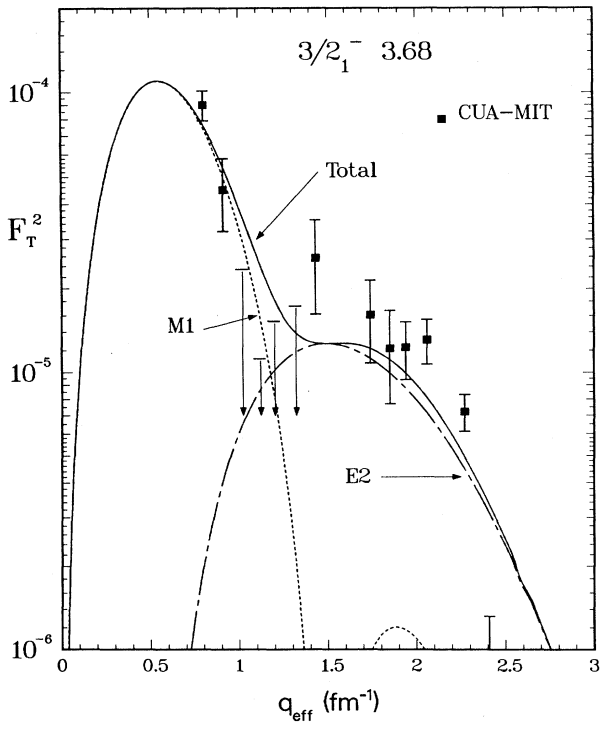

FIG. 16. The transverse form factor for the $\frac{3}{2}^-$ 3.68 MeV level. The shell-model form factors are calculated using Woods-Saxon radial wave functions. The $M1$ transition strength is scaled down by a factor of 0.53 to reproduce the experimental $B(M1)$ value.

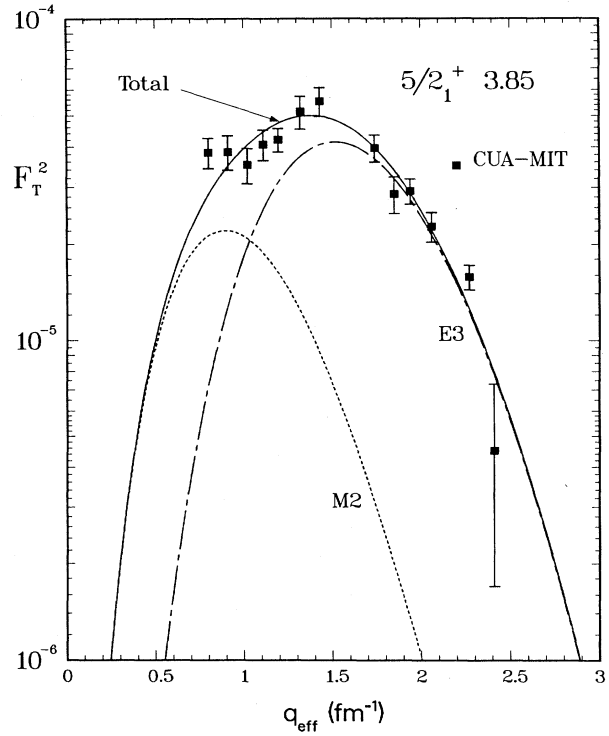

FIG. 17. The transverse form factor for the $\frac{5}{2}^+$ 3.85 MeV level. The shell-model form factors are calculated using Woods-Saxon radial wave functions. The $M2$ transition strength is scaled down by a factor of 0.59 to reproduce the experimental $B(M2)$ value. The magnetization current amplitude for the $E3$ contribution is scaled by 0.707.

function into the $5/2_2^+$ model wave function would lead to improved agreement with the data. Figure 19(b) shows the form factor which results when the $5/2_1^+$ level is admixed with an amplitude of 0.3. The resultant $M2$ form factor reproduces the data rather well (the spin contribution to the $E2$ form factor has been renormalized by a factor of 0.707). An added bonus is that the $C3$ form factor, which is negligibly small for the pure $5/2_2^+$ model state, now matches the data in Fig. 9. The $C3$ and $E3$ form factors for the orthogonal linear combination, now the wave function for the 3.85 MeV level, are slightly reduced. The $B(M2)$ is increased, but the $M2$ form factor peaks at lower q and drops off more quickly at high q because the $(\lambda\mu)=(10)$ amplitude is increased relative to $(\lambda\mu)=(21)$.

4. *The 7.55 MeV complex*

As stated in Sec. V, the $\frac{7}{2}^+$ 7.49 MeV, $\frac{5}{2}^-$ 7.55 MeV, and $\frac{3}{2}^+$ 7.69 MeV levels are never clearly resolved. The 7.55 MeV level is the dominant state in the complex, as can be seen from Fig. 20. The $E2$ form factor arises predominantly from $p_{1/2}\leftrightarrow p_{3/2}$ proton excitations, and the $M3$ form factor is negligibly small (1.5×10^{-6} at peak). As for the $\frac{3}{2}^-$ 3.68 MeV level, there is some sensitivity to cancellations between neutron contributions based on widely separated core states, but it is less severe in this case. In calculating the $E2$ form factor, the continuity equation (15) has been used for the convection current, and the magnetization current contribution has been scaled by the factor 0.707. The theoretical curve lies below the data at high q. However, we expect the core polarization corrections which reduce the magnetization current contributions to change the shape of the form factor such that it holds up at high q. This behavior is clearly evident from the U Mass data,[7] and is reproduced for several similar $E2$ transitions in the core polarization calculations of Sato *et al.*[59] The U Mass data is for the unresolved set of levels, and could contain contributions from the $\frac{7}{2}^+$ and $\frac{3}{2}^+$ levels. Since the $7/2_1^+$ state has a simple structure and no other $\frac{7}{2}^+$ levels are close in energy, we believe that the form factor can be estimated quite reliably if effective g factors are used. For the curves in Fig. 20, the $E3$ magnetization current has been reduced by 0.707, and the $M4$ by the factor 0.91 required for the $\frac{9}{2}^+$ 9.50 MeV level.[8] For $q>1.6$ fm^{-1}, the form factor of the $\frac{7}{2}^+$ level can make a significant contribution to the total transverse form factor of the complex. A better estimate, which would enhance the $\frac{7}{2}^+$ form factor at high q, could have been made by using a Woods-Saxon well with a smaller radius, as is required to reproduce[8] the high q behavior of the form factor of the $\frac{9}{2}^+$ 9.50 MeV state. The difficulty of trying to extract form factors for the weaker levels in the complex is evident from the scatter in the data points for the $\frac{7}{2}^+$ level in Fig. 20.

For the $\frac{3}{2}^+$ 7.69 MeV level, we expect our calculations to be much less reliable, partly because $E1$ and $M2$ form factors can exhibit a wide variety of shapes and partly because another $\frac{3}{2}^+$ level exists nearby. The other $\frac{3}{2}^+$ level

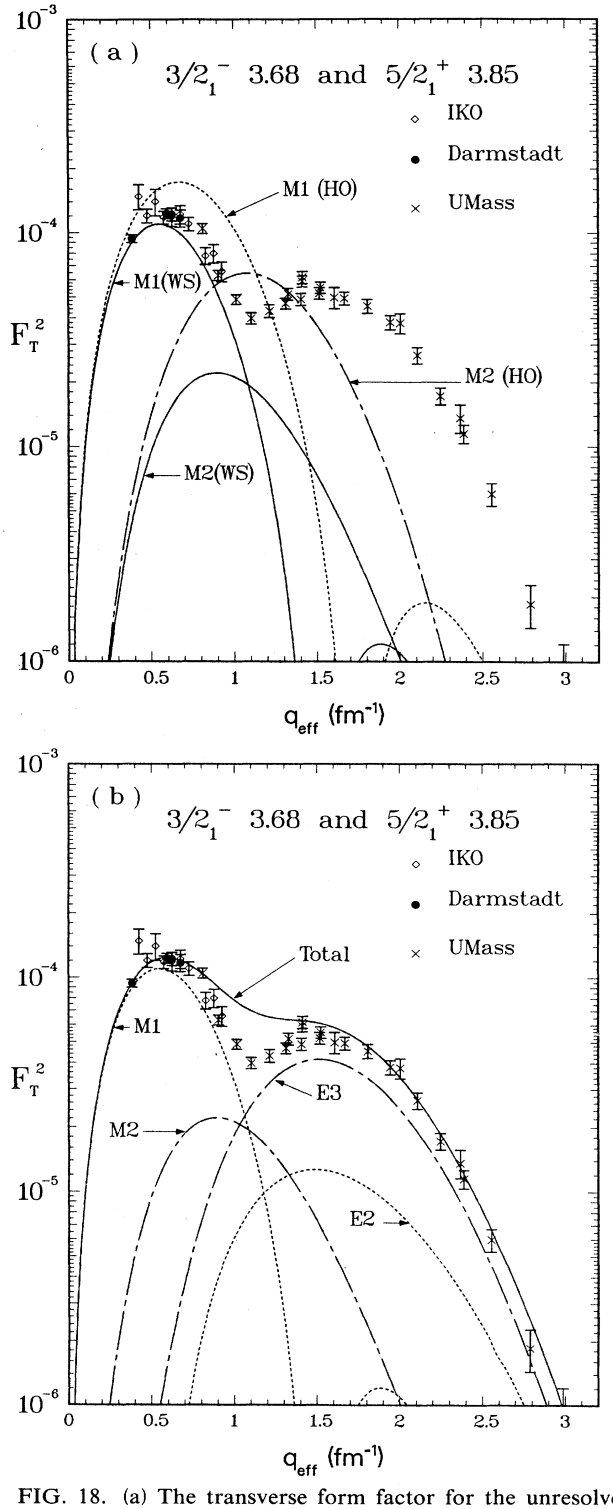

FIG. 18. (a) The transverse form factor for the unresolved $\frac{3}{2}^-$ 3.68 MeV and $\frac{5}{2}^+$ 3.85 MeV levels. Shell-model form factors calculated using Woods-Saxon and harmonic oscillator radial wave functions are compared. The $M1$ and $M2$ transition strengths are scaled to reproduce the experimental $B(M1)$ and $B(M2)$ values. (b) All contributions to the transverse form factor of the unresolved doublet, calculated with the renormalizations given in the text and the captions to Figs. 16 and 17, are shown. Woods-Saxon wave functions are used.

is the very broad 8.20 MeV level which contains a significant fraction of ^{12}C g.s.$\times d_{3/2}$ strength. Our predicted form factors for both $\frac{3}{2}^+$ levels are shown in Fig. 21, along with the data extracted for the 7.69 MeV level. The data shows that $F_T^2 < 10^{-5}$ for all q. The predicted $M2$ form factor for the first $\frac{3}{2}^+$ level is very small (5×10^{-7} at peak) and is not shown. The corresponding $E1$ form factor is consistent with the data at the highest- and lowest-momentum transfers. The $M2$ form factor for the second $\frac{3}{2}^+$ model state is relatively large, which suggests admixing a little of the $3/2_2^+$ state into the wave function for the 7.69 MeV level in order to fill in the minimum of the $E1$ form factor. The curves labeled (+) and (−) in Fig. 21 show the result of admixing at 0.3 amplitude with positive and negative sign, respectively. There are reasons, discussed herein, to prefer the (+) case. In any event, the form factor is big enough at large q to give a contribution to the combined form factor in Fig. 20 which is comparable to that expected for the $\frac{7}{2}^+$ level.

Our reasons for preferring the (+) case of mixing are based on the observed particle decay widths[6] of the $\frac{3}{2}^+$ levels, 70 and 115 keV for $3/2_1^+$ in ^{13}C and ^{13}N, respectively (1000 and $\sim$1500 keV for $3/2_2^+$). The calculated widths of single-particle resonances in our potential wells are 613, 1284, 911, and 2263 keV for the four cases in the order above. The theoretical spectroscopic factors, $(13/12)^2$ times the square of the $0^+\times\frac{3}{2}$ amplitudes listed in Table II, are 0.014 and 0.687 for $3/2_1^+$ and $3/2_2^+$, respectively. Clearly, only the admixture of $3/2_2^+$ into $3/2_1^+$ with positive amplitude increases the $d_{3/2}$ spectroscopic amplitude for the lower state sufficiently to approach the observed width (the $2^+\times s_{1/2}$ component also contributes significantly to the width in ^{13}N) and spectroscopic factor.[60] The model states are actually predicted too close together (Table II), so that some "unmixing" could be expected when energies are fine tuned. About 75% of the $\frac{3}{2}^+$ wave functions comes from approximately orthogonal admixtures of $(\lambda\mu)=(24)$, $L=2$, $S=\frac{1}{2}$ configurations with $K=0$ and $K=2$ (the same is true for $5/2_1^+$ and $5/2_2^+$), and, in the (+) case, the mixing of $K=0$ and $K=2$ is reduced. However, we caution that a two-state mixing argument is certainly too simplistic, as can be seen from the weak-coupling decomposition in Table II. In fact, only 65% of the available $d_{3/2}$ strength is accounted for by the first two model states.

5. *The $\frac{1}{2}^-$ 8.86 MeV level*

The Woods-Saxon form factor squared for the $1/2_2^-$ model state, scaled by a factor of 0.48, is compared with the data in Fig. 22. This is mainly a $p_{1/2}\leftrightarrow p_{3/2}$ proton transition. The p-shell wave functions overestimate the $B(M1)$ value by a factor of 2. Use of the effective g factors of Towner and Khanna[58] reduces the $B(M1)$ by 18%. The measurement of Holt *et al.*,[61] listed in Table V, is inconsistent with the (e,e') measurements, which are reasonably consistent with each other.

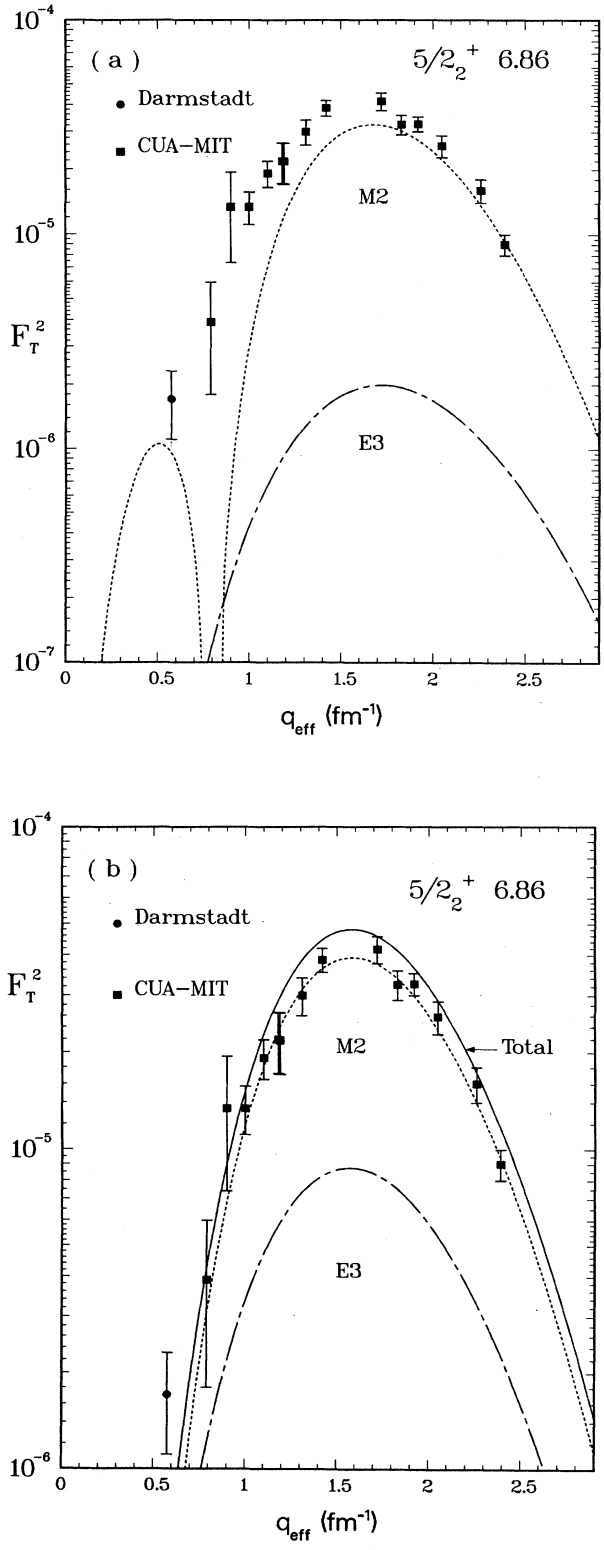

FIG. 19. (a) The transverse form factor for the $\frac{5}{2}^+$ 6.86 MeV level. The shell-model form factors are calculated using Woods-Saxon radial wave functions. No renormalizations are applied. (b) The shell-model transverse form factors for a 91% to 9% mixture of second and first $\frac{5}{2}^+$ model wave functions. The $E3$ spin amplitude is scaled by 0.707.

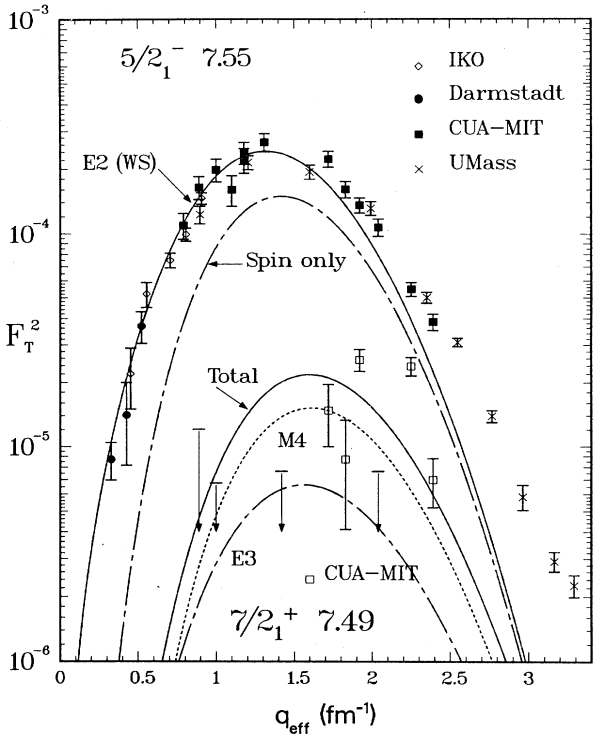

FIG. 20. Transverse form factors for the unresolved triplet consisting of the $\frac{7}{2}^+$ 7.49 MeV, $\frac{5}{2}^-$ 7.55 MeV, and $\frac{3}{2}^+$ 7.69 MeV levels. The CUA data result from an attempt to separate the contributions from the individual levels. The magnetization current amplitudes to the $E2$, $E3$, and $M4$ transitions are scaled by 0.707, 0.707, and 0.91, respectively.

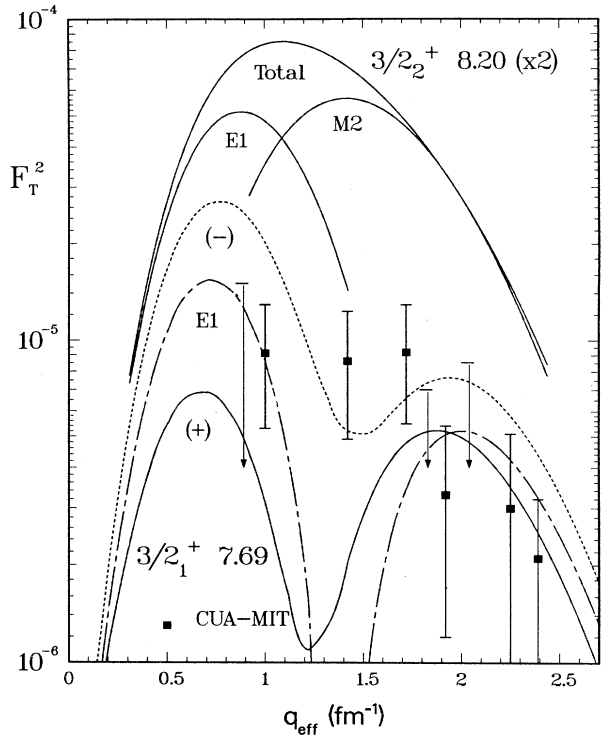

FIG. 21. The contribution of the $\frac{3}{2}^+$ 7.69 MeV level to the transverse form factor of the 7.55 MeV complex. The theoretical curves are discussed in Sec. V F 4. Also shown is the theoretical prediction for the $\frac{3}{2}^+$ 8.2 MeV level, which is very broad and is not observed in the experiments.

6. *The $\frac{9}{2}^+$ 9.50 MeV level*

The data for this level have been published and fully discussed elsewhere.[8] It is worth mentioning that the shell-model form factor lies above the data in common with the magnetization current contributions for other multipoles. The quenching of F_T^2 for the 9.50 MeV is somewhat less than the factor of 2 which is typically required for strong isovector $M4$ transitions.[8] Also, F_T^2 holds up at high q in a manner consistent with other spin transitions. In Ref. 8, a harmonic oscillator parameter $b=1.53$ fm or a Woods-Saxon well parameter $r_{on}=1.15$ fm was used to parametrize the shape of the form factor.

7. *The $\frac{3}{2}^-$ 9.90 MeV and $\frac{1}{2}^-$ 11.08 MeV levels*

The $B(M1)$ values for these two levels are considerably smaller than those measured for any of the basically p-shell levels (Table V), which is consistent with our identification of these states as being mainly of $p^7(sd)^2$ structure. The squared $M1$ form factors[3] reach $\sim 5\times 10^{-6}$ at $q_{eff}=0.54$ fm^{-1}. For the 9.90 MeV level, our IKO data gives upper limits about a factor of 2 above the Darmstadt data[3] for three points in the range

$$0.4 \text{ fm}^{-1} < q_{eff} < 0.65 \text{ fm}^{-1} .$$

There are two 180° U Mass data points[7] at $E_x=11.0$ MeV for $q_{eff}=1.59$ and 1.97 fm^{-1}, with F_T^2 equal to $1.33(55)\times 10^{-5}$ and $1.51(30)\times 10^{-5}$, respectively. We interpret these points as due to the excitation of the $\frac{1}{2}^+$ level[6] at 10.996 MeV, and have used them to subtract the transverse contribution from our 90° data in order to obtain F_L^2 for the $\frac{1}{2}^-$ 11.08 MeV level. As was indicated in the discussion of longitudinal form factors, the $1/2_2^+$ model state does not appear to be a good candidate for the 10.996 MeV level. The transverse form factor of the $1/2_2^+$ model state is interesting in that it has a large convection current contribution from the dominant $(\lambda\mu)=(21)$, $\Delta S=0$ OBDME (Table III), which by itself gives rise to a $C2$ shaped form factor with a maximum value of 10^{-5}. The magnetization current contribution is not dominant because the relevant $\Delta S=1$ OBDME are both small and isoscalar (Table III). Above $q=1.1$ fm^{-1} there is destructive interference, and the form factor drops very rapidly. The peak, still at 10^{-5}, shifts to $q=0.95$ fm^{-1} and by $q=2$ fm^{-1} F_T^2 is less than 10^{-7}, way below the U Mass data point. Also, at low q, F_T^2 is comparable to the $M1$ form factor observed at Darmstadt.[3]

8. *The 11.8 MeV complex*

The strong longitudinal $C3$ form factors of the $\frac{7}{2}^+$ 11.85 MeV and $\frac{5}{2}^+$ 11.95 MeV levels were discussed in Sec. V E 3. At low q we expect F_T^2 for the unresolved

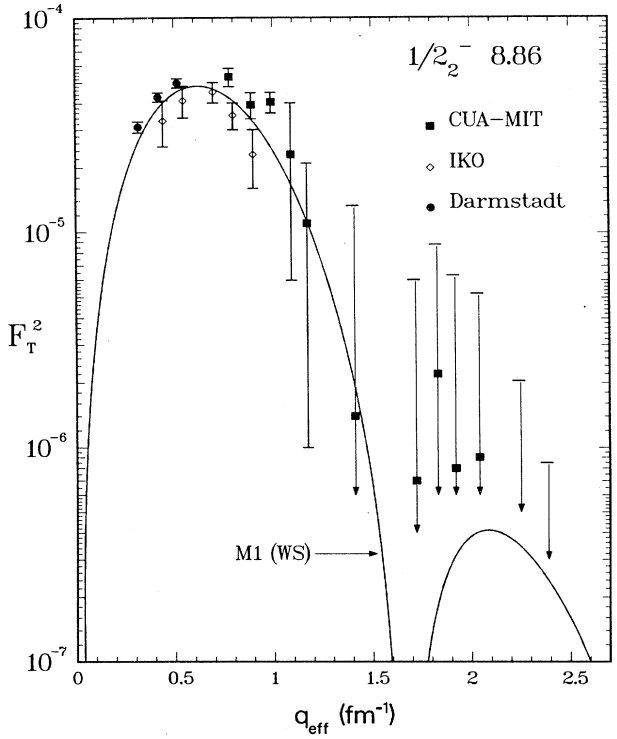

FIG. 22. The transverse form factor for the $\frac{1}{2}^-$ 8.86 MeV level. For $q_{\text{eff}} > 1.3$ fm^{-1}, only upper limits can be given (see caption to Fig. 4). In these cases, the value obtained from the Rosenbluth separation is given if the value of F_T^2 is greater than zero. The shell-model form factors are calculated using Woods-Saxon radial wave functions. The $M1$ transition strength is scaled down by a factor of 0.48 to reproduce the experimental $B(M1)$ value.

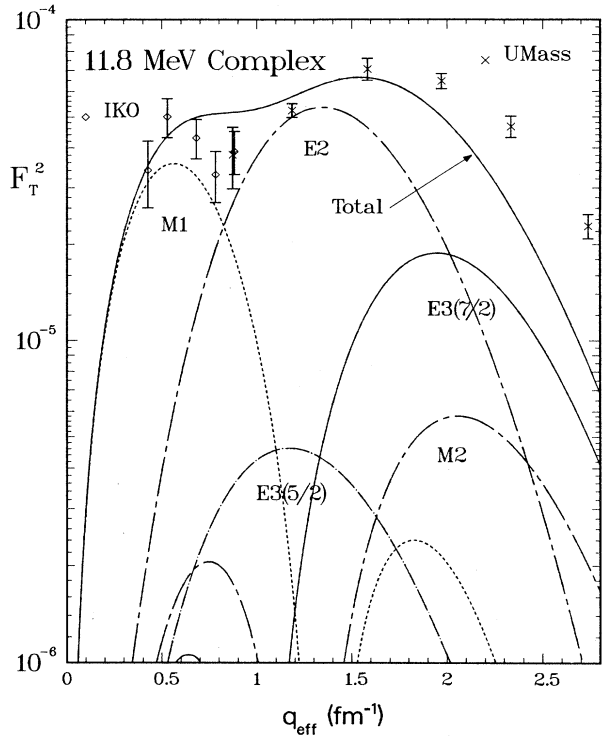

FIG. 23. Transverse form factors for the 11.8 MeV complex consisting of the $\frac{3}{2}^-$ 11.75 MeV, $\frac{7}{2}^+$, 11.85 MeV, and $\frac{5}{2}^+$ 11.95 MeV levels. The shell-model form factors are calculated using Woods-Saxon radial wave functions. The $M1$ transition strength is scaled down by a factor of 0.72, and the magnetization current contribution to the $E2$ transition is scaled by a factor of 0.707.

triplet of levels to be dominated by the $M1$ form factor of the $\frac{3}{2}^-$ 11.75 MeV state. Our IKO data, shown in Fig. 23, define the magnitude of the peak of the $M1$ form factor quite well, although $E2$ contributions may be significant. $F_T^2(M1)$ has been scaled down by a factor of 0.72 to aid the comparison of the theoretical curves with the data. The effective g factors of Towner and Khanna[58] give just this reduction for the dominantly $p_{1/2} \leftrightarrow p_{3/2}$ transition associated with the second $\frac{3}{2}^-$ p-shell model state. The $E2$ form factor was evaluated by scaling the magnetization current contribution by the usual factor of 0.707. The experimental F_T^2 appears to be quite well defined at intermediate and high q by the U Mass data points. The major contributions to the form factor are expected from the $E2$ form factor of the $\frac{3}{2}^-$ 11.75 MeV level, the $E3$ form factor of the $\frac{7}{2}^+$ 11.85 MeV level, and the $M2$ form factor of the $\frac{5}{2}^+$ 11.95 MeV level. Looking at the various contributions in Fig. 23, it appears that the $E2$ contribution may be slightly overestimated and the others underestimated. Some of the observations made in the preceding section concerning F_T^2 for the $1/2_2^+$ model state are also relevant to the $E3$ form factors. For example, the strong isoscalar $\Delta S=0$ OBDME mean that convection currents play an important role. Indeed, for the $5/2_4^+$ state the $\Delta L=3$, $\Delta S=1$ OBDME are tiny, and the form factor has a $C2$ shape. For the $7/2_2^+$ state, the spin contribution is larger, but not dominant until high q, and interferes destructively with the orbital contribution, giving rise to a minimum at $q=1$ fm^{-1}. No renormalization of the spin contribution has been made in Fig. 23. If the quenching of a factor of 0.707 is applied, $F_T^2(E3)$ drops to 7.4×10^{-6} at $q=2$ fm^{-1}. For the $M2$ form factor the interference between $\Delta S=0$ and $\Delta S=1$ is destructive at the first maximum and constructive at the second maximum. The $M4$ contribution from the $\frac{7}{2}^+$ level is included in the total, but it is predicted to be quite small. $F_T^2(M4)$ reaches a peak value a little greater than 10^{-6}. In summary, the measured F_T^2 at high q is somewhat larger than the model wave functions for the $\frac{7}{2}^+$ and $\frac{5}{2}^+$ give. However, it is clear that a modest increase in the $M2$ and $E3$ strength, together with an allowance for the empirically observed shape discrepancy of the $E2$, in particular, at high q, could account for the data.

9. *The $\frac{3}{2}^-$ 15.11 MeV level*

The transverse form factor for the first $T=\frac{3}{2}$ level of ^{13}C is shown in Fig. 24. The $M1$ contribution is not re-

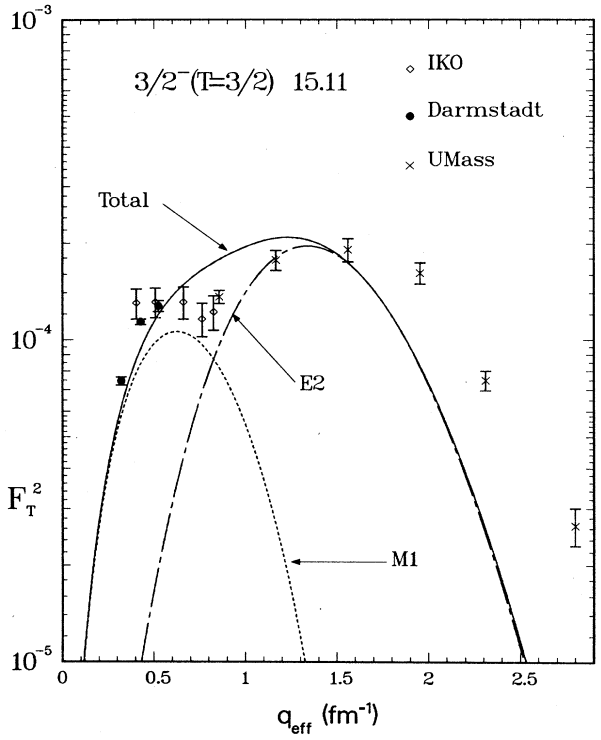

FIG. 24. The transverse form factor for the $\frac{3}{2}^-$ 15.11 MeV level. The shell-model form factors are calculated using Woods-Saxon radial wave functions. The $M1$ transition strength is not scaled, and the magnetization current contribution to the $E2$ transition is scaled by a factor of 0.707.

normalized, and the magnetization current contribution to the $E2$ form factor is reduced by a factor of 0.707. The magnitude of the F_T^2 which results is about right, except at high q. Calculations by Sato *et al.*,[59] which include core polarization corrections up to $6\hbar\omega$, much improve the magnitude and q dependence of $F_T^2(E2)$ compared with that of the unrenormalized p-shell $E2$ form factor. The use of Woods-Saxon instead of HO wave functions leads to significant changes in the shape and magnitude of the $M1$ and $E2$ form factors (see Table VI), which is not surprising given the large difference in separation energies from the initial and final states. The predicted $F_T^2(M1)$ is compatible with, perhaps a little below, the data. The effective g factors of Towner and Khanna[58] reduce the $B(M1)$ value by a further 18%. Thus, we have a situation in which the p-shell model gives $B(M1)$ values for the excitation of the $\frac{3}{2}^-$ 3.68 MeV and $\frac{1}{2}^-$ 8.86 MeV states which are too large by about a factor of 2, while those for the $\frac{3}{2}^-$ 11.75 MeV and $\frac{3}{2}^-$ 15.11 MeV states are compatible with the data. All the transitions are predominantly $p_{1/2}\leftrightarrow p_{3/2}$ (in the combination $\frac{3}{2}\frac{1}{2}-\frac{1}{2}\frac{3}{2}$), so it is clear that an effective $M1$ operator for use with the Cohen and Kurath wave functions cannot be found. In contrast, the work of Brown and Wildenthal[62] has achieved a successful matching of effective $M1$ and Gamow-Teller[63] operators with an effective interaction in the *sd* shell. The situation regarding the $M1$ transitions in ^{13}C is typical of the p shell. If the $\sigma\tau$ part of the $M1$ operator dominates, the $M1$ transition from the $\frac{3}{2}^-$ 15.11 MeV state, to take a specific example, proceeds via the admixtures of [432] spatial symmetry in the ground state. Thus, there is great sensitivity of the SU4 symmetry-breaking characteristics of the effective interaction including, particularly, the strength of the one-body spin-orbit interaction. This suggests that the effective interaction and the effective one-body operators should be fitted simultaneously to energy and transition data. Recently, such an approach, which includes energy level and static momenta data, has been taken for the p shell.[64]

VI. SUMMARY AND DISCUSSION

We have compared experimental longitudinal and transverse form factors, obtained for many levels of ^{13}C below 12 MeV excitation energy, with theoretical form factors computed using effective one-body operators, Woods-Saxon radial wave functions, and the one-body density matrix element from $0\hbar\omega$ and the $1\hbar\omega$ shell-model calculations for the negative- and positive-parity, levels respectively.

For longitudinal $C2$ and $C3$ transitions, a good description of the data for momentum transfers below the peaks of the form factors is obtained with fixed effective charges. The effective charges are similar for the two multipoles, $e_0\sim 1.6e$ and $e_1\sim 0.7e$, and work well universally for light nuclei. As expected, the radial transition densities from the lowest-order shell model are inadequate to explain the shape of the associated form factors at higher-momentum transfers. We chose to present our comparison between experiment and theory in such a way as to emphasize the fact that the form factor shapes deviate from the lowest-order shell-model prediction in a way as regular as the magnitudes. This demonstration is made possible by the availability of data which define the form factors with precision over a wide range of momentum transfers. The differences between the enhanced shell-model transition densities and the fits to the data bear a qualitative resemblance to the surface peaked transition densities associated with admixtures of giant quadrupole or octupole resonances into the low-lying states, and it is clear that phenomenological effective one-body operators which incorporate these effects, and thus work for a wide range of momentum transfers, can be defined.

The situation for $C1$ transitions between low-lying levels is quite similar, with the need for enhancement in magnitude and compression of the form factor in momentum space again being a regular feature for light nuclei. Here, there are the special features that the $C1$ matrix element is small and that the single particle transitions through three shells can be particularly effective in enhancing the $C3$-like peak of the form factor. Unfortunately, the fact that the lowest $\frac{3}{2}^+$ level in ^{13}C could not be properly resolved from the strongly excited $\frac{5}{2}^-$ level at 7.55 MeV left only a single $C1$ transition that could be studied in detail. For levels with appreciable $C1$ matrix elements, a variety of form factor shapes are possible depending on the magnitude and interference prop-

erties of the basic $(\lambda\mu)=(10)$ and (21) amplitudes (specific linear combinations of $0p \rightarrow 1s$ and $0p \rightarrow 0d$). Usually, such states occur at relatively high excitation energies and may be broad, or at least difficult to resolve from other broad states nearby.

Two $C0$ transitions have been observed in ^{13}C and the form factor of the $\frac{1}{2}^-$ 8.86 MeV level, in particular, is well defined by the present data set. The transitions are quite strong and typical of $C0$ transitions in light nuclei. The $C0$ form factors are difficult to calculate, and we have noted that the different intrinsic spins which dominate in the model wave functions for the transition to the 8.86 MeV level pose a particular problem in understanding the strength of the transition.

The transverse form factors are, in some respects, more interesting probes of the underlying single-particle structure of states in ^{13}C because the magnetization density of the odd neutron is probed. This feature is most clearly evident for low multipolarity $E1$ and $M2$ transitions to the low-lying $\frac{1}{2}^+$, $\frac{3}{2}^+$, and $\frac{5}{2}^+$ states, which have basically the simple structure of a neutron coupled to the ^{12}C core. The form factors can exhibit a wide variety of shapes, depending on the interference of $0p \rightarrow 1s$ and $0p \rightarrow 0d$ amplitudes and on the interference of convection and magnetization current contributions. For the low-lying states, the odd-neutron structure limits the role played by convection currents. The excitation of the $\frac{1}{2}^+$ 3.09 MeV level provides a clear example of a $0p \rightarrow 1s$ $E1$ transition with $0p \rightarrow 0d$ neutron and convection current amplitudes proving crucial to the description of the first maximum and the minimum at low q. For the loosely bound neutron orbits, it makes little sense to use harmonic oscillator wave functions. In fact, the transverse form factors calculated with Woods-Saxon wave functions are usually considerably reduced in magnitude, and differ significantly in shape, from those calculated with harmonic oscillator wave functions.

The SU3 LS classification provides a useful alternative basis for the OBDME. The size of convection $(\Delta S=0)$ and magnetization $(\Delta S=1)$ current contributions is immediately apparent. Furthermore, the SU3 classification separates, independently of multipolarity, form factor amplitudes which peak at low $[(\lambda\mu)=(10)]$ or high $[(\lambda\mu)=(21)]$ momentum transfers. The form factors for the transition to the $\frac{5}{2}^+$ 6.86 MeV provide an interesting example in which the (21) $\Delta S=1$, $\Delta T=1$ amplitude dominates. Nevertheless, a small (10) amplitude for the $5/2_2^+$ model state produces a minimum at low q [Fig. 19(a)]. However, a small empirical admixture of the $5/2_1^+$ model state wave function wipes out the (10) amplitude and leads to an $M2$ form factor which has the same shape as the $E3$ form factor [Fig. 19(b)], which is uniquely due to a (21) OBDME. In general, two multipolarities contribute to each transition and, as in the previous example, it may not be possible to distinguish them on the basis of the shape of the measured form factor. A more obvious example occurs in the case of $E3$ and $M4$ transitions, unless there are large convection current contributions to the $E3$. The $5/2_4^+$ model state, identified with the 11.95 MeV level, provides an unusual example in which the convection current contribution to the $E3$ transition dominates, leading to a form factor with the same shape as a $C2$ form factor. Unfortunately, the 11.95 MeV level is a member of an unresolved complex, so this model prediction is not tested by the present data.

The higher $E2$, $E3$, and $M4$ multipole transition strengths are generally overestimated by the lowest-order ($0\hbar\omega$ and $1\hbar\omega$) shell-model calculations. As a general rule, a reduction of the strength due to the magnetization current by a factor 2 much improves the agreement with experiment. This is roughly equivalent to the use of an effective isovector g factor which is 0.7 times the free nucleon value (cf. the $C2$ and $C3$ isovector effective charges). If the reduction in magnitude is attributed to core polarization effects involving higher shell-model orbits, we would expect the transverse form factors for these multipoles to be enhanced at high q as is indeed observed. In fact, the high-q enhancement is very striking[10]

TABLE VII. Basic SU3 shell-model form factors.[a]

				$0p \rightarrow 0s\,(10)$	$1s0d-0p\,(10)$	$1s0d-0p\,(21)$
	Common factor			1	$1-\frac{1}{2}y$	y
$\Delta J=1$	L[b]	$\Delta L=1$	$\Delta S=0$	$\sqrt{2}/\sqrt{3}y^{1/2}$	$2\sqrt{2}/\sqrt{3}y^{1/2}$	$-\sqrt{2}/\sqrt{3}\sqrt{5}y^{1/2}$
	T	$\Delta L=1$	$\Delta S=0$	$-2/\sqrt{3}$	$-4/\sqrt{3}$	$-2\sqrt{3}/\sqrt{5}$
	T	$\Delta L=1$	$\Delta S=1$	c	c	c
$\Delta J=2$	T	$\Delta L=2$	$\Delta S=0$			$-4\sqrt{2}/\sqrt{3}\sqrt{5}$
	T	$\Delta L=1$	$\Delta S=1$	$-2\sqrt{2}/\sqrt{5}y$	$-4\sqrt{2}/\sqrt{5}y$	$2\sqrt{2}/5y$
	T	$\Delta L=3$	$\Delta S=1$	$8/5\sqrt{7}y$		
$\Delta J=3$	L	$\Delta L=3$	$\Delta S=0$			$-2\sqrt{2}/\sqrt{5}\sqrt{7}y^{1/2}$
	T	$\Delta L=3$	$\Delta S=0$			$4\sqrt{2}/\sqrt{3}\sqrt{5}\sqrt{7}$
	T	$\Delta L=3$	$\Delta S=1$			c
$\Delta J=4$	T	$\Delta L=3$	$\Delta S=1$			$4\sqrt{2}/3\sqrt{7}y$

[a]Given as ZFe^y or $ZFe^y(b/\mu_B)$.
[b]$L \equiv$ longitudinal, $T \equiv$ transverse
[c]$2y^{1/2}$ times entry for longitudinal two lines above.

TABLE VIII. Measured form factors squared for states of ^{13}C.

E_0 (MeV)	θ (deg)	Elastic[a]	3.088[b]	3.684[b]	3.854[b]	6.864[b]	7.492[b]	7.547[b]	7.667[b]	8.860[b]	9.500[b]	9.897[b]
129.4	45	570(29)	2.13(56)	8.23(73)	0.00(82)			12.68(74)		2.79(43)	0.00(28)	0.47(27)
156.4	45	459(23)	2.76(49)	14.0(1.0)	0.96(44)			21.0(1.2)				
180.0	45	368(19)	3.71(73)	22.3(1.2)	2.11(32)			31.7(1.7)				
206.0	45	256(13)	3.24(35)	28.3(1.5)	1.64(28)	0.32(20)		42.1(2.2)		4.82(46)	0.28(15)	0.53(16)
125.4	90	209(12)	3.63(35)	40.7(2.4)	2.37(28)	0.22(18)	0.05(24)	52.9(3.1)	0.30(38)	6.70(53)	0.34(13)	0.82(14)
140.9	90	118.3(6.0)	2.7(1.1)	43.3(2.2)	3.49(25)	0.21(17)	0.06(23)	65.3(3.3)	0.71(30)	6.30(47)	0.32(13)	0.89(15)
155.2	90	75.6(4.4)	4.33(30)	48.5(2.9)	4.35(32)	0.66(14)		74.8(4.4)		7.71(46)	0.59(13)	1.37(20)
165.7	90	47.6(2.4)	3.59(22)	45.1(2.3)	4.51(28)	0.684(81)	0.21(12)	70.8(3.6)	0.36(15)	5.56(33)	0.811(89)	1.35(11)
167.3	90	48.5(2.8)	4.15(27)	46.9(2.8)	4.61(31)	0.717(82)		76.5(4.5)		6.00(39)	1.26(11)	1.72(13)
184.8	90	20.2(1.0)	3.28(24)	36.0(1.9)	5.19(38)	0.85(13)		65.3(3.3)				
200.3	90	8.21(41)	3.07(16)	34.2(1.7)	5.33(43)	0.808(77)	1.87(65)	58.3(2.9)	0.34(12)	2.81(17)		
221.3	90	1.731(89)	2.27(14)	25.8(1.3)	5.10(30)	0.812(79)		41.7(2.2)			2.40(19)	
221.3	90	1.838(93)	2.36(14)	25.0(1.3)	4.91(27)	0.827(62)	1.16(13)	41.8(2.1)	0.026(89)	1.23(19)	1.96(12)	0.87(11)
243.3	90	0.1167(84)	1.53(11)	15.78(94)	4.11(27)	0.887(84)	0.90(10)	27.7(1.6)	0.00(11)	0.37(14)	1.89(14)	0.646(67)
259.3	90	0.0931(65)	1.113(78)	10.14(60)	3.02(19)	0.708(70)	0.60(11)	18.1(1.1)	0.41(11)	0.30(14)	1.94(14)	0.368(44)
271.4	90	0.251(15)	0.923(74)	7.79(47)	2.52(17)	0.675(64)	0.00(11)	12.92(78)	0.563(92)	0.236(70)	1.83(12)	0.262(45)
276.8	90	0.303(16)	0.797(54)	6.19(32)	2.16(13)	0.63(11)	1.01(14)	10.86(57)	0.19(11)	0.25(16)	1.77(10)	0.240(36)
289.6	90	0.403(21)	0.577(36)	3.81(20)	1.590(85)	0.491(32)	0.343(35)	7.24(37)	0.174(28)	0.068(24)	1.506(81)	0.166(20)
319.4	90	0.422(22)	0.313(21)	1.060(60)	0.730(43)	0.261(27)	0.413(43)	2.36(13)	0.112(31)	0.062(22)	1.151(64)	0.104(19)
339.1	90	0.300(15)	0.195(14)	0.366(24)	0.366(25)	0.183(15)	0.181(25)	1.078(64)	0.019(15)	0.058(13)	0.875(50)	0.025(10)
78.1	160	268(14)	4.0(1.3)	57.1(3.3)	13.9(1.3)	1.58(65)		77.1(4.2)		21.8(1.6)	2.41(65)	0.61(56)
90.0	160	192.8(9.9)	3.7(1.4)	54.8(3.3)	14.4(1.4)	4.4(1.9)	0.8(1.4)	103.9(5.5)	1.9(1.5)	18.9(1.6)	5.67(67)	1.77(51)
100.2	160	113.4(5.9)	0.1(2.5)	43.6(2.8)	14.5(1.3)	4.38(68)	0.0(1.0)	127.2(6.7)	3.5(1.1)	18.9(1.3)	6.45(65)	0.57(41)
110.1	160	71.7(3.7)	3.74(62)	43.7(2.7)	17.0(1.3)	6.64(83)		124.8(6.7)		14.2(5.1)	10.4(1.0)	1.89(58)
118.7	160	42.1(2.2)	5.25(76)	42.6(2.8)	17.7(1.5)	7.5(1.5)		145.1(8.0)		9.0(3.2)	16.2(1.5)	0.53(59)
130.9	160	20.4(1.1)	5.89(86)	34.3(3.0)	21.2(1.8)	10.2(1.2)		148.2(8.2)		42(15)	25.9(2.0)	1.47(75)
142.6	160	8.86(47)	9.66(71)	42.2(2.4)	22.6(1.7)	12.9(1.0)	1.7(1.3)	144.8(7.7)	3.0(1.2)	3.2(1.8)	33.5(1.9)	0.2(2.9)
174.0	160	0.712(55)	9.51(76)	20.8(1.4)	16.5(1.1)	13.9(1.2)	5.5(1.5)	97.2(5.8)	3.0(1.2)	0.60(78)	45.2(2.8)	1.04(53)
185.1	160	0.779(83)	8.72(91)	14.0(1.3)	11.9(1.2)	10.8(1.1)	3.3(1.4)	68.3(4.3)	0.57(98)	0.98(98)	45.8(3.2)	0.02(63)
194.7	160	0.884(61)	9.50(65)	11.62(78)	11.62(79)	10.83(81)	8.0(1.2)	55.4(3.2)	1.59(64)	0.49(85)	37.9(2.2)	0.27(39)
206.9	160	0.877(72)	7.76(69)	7.90(71)	8.67(75)	8.52(93)	0.4(1.2)	40.6(3.0)	0.97(92)	0.34(69)	31.7(2.3)	0.00(38)
228.8	160	0.891(58)	5.66(41)	3.32(32)	5.65(43)	5.26(61)	7.85(76)	19.4(1.3)	1.03(35)	0.00(33)	28.6(1.6)	0.39(35)
243.0	160	0.562(46)	4.28(40)	0.63(15)	1.76(88)	2.99(32)	2.37(57)	13.1(1.1)	0.67(35)	0.00(16)		

[a] $F^2\times10^3$ is given for elastic scattering. The errors in the last significant figures are given in parentheses.
[b] Level energies in MeV. $F^2\times10^4$ is given for excited states.

and is not fully understood. In contrast to the core polarization effects for longitudinal multipoles, the *NN* tensor force, which connects to high-energy intermediate states, plays an important role for transverse multipoles. There have been many calculations (Ref. 59 and references contained therein) for ^{12}C and ^{13}C, mostly for the $M1$ multipole, which evaluate both core polarization and exchange current effects for intermediate states up to $6\hbar\omega$ or even higher. Generally, core polarization effects are much larger than exchange current or delta isobar effects, especially for higher multipoles. However, the effect of exchange currents is to enhance the form factors at high-momentum transfer.

We regard the description of the comprehensive set of form factors, obtained in our ^{13}C$(e,e')^{13}$C experiment, by the lowest-order shell-model as quite satisfactory when effective one-body operators are used. For the lowest pairs of $\frac{3}{2}^+$ and $\frac{5}{2}^+$ states, a small mutual admixing of the model states would lead to improved agreement with experiment. We have been able to to provide an understanding of the structure of the states near 11.9 MeV excitation energy which are strongly excited by the inelastic scattering of electrons and hadronic probes. The shell-model analysis is simplified by the fact that multiparticle-multihole configurations do not appear to play a role at low excitation energies in ^{13}C. The levels that we have identified as due to the promotion of two particles from the *p* shell to the *sd* shell are quite weakly excited. The transitions of $M1$ and $C0$ multipolarity

TABLE IX. ^{13}C excitation energies and widths determined in this experiment.[a]

Energy[b] (MeV)	Width[c] (keV)
9.500(7)	
11.845(5)	144(5)
12.187(10)	109(48)
12.438(12)	160(37)
14.390(15)	281(65)
14.582(10)	227(41)
14.983(10)	380(53)
15.526(11)	147(23)
16.080(7)	148(13)
[16.183(28)	40(20]
[18.497(10)	91(23)]
18.699(5)	98(11)
20.021(13)	232(27)
20.429(8)	112(23)
21.466(8)	268(14)

[a]Only levels observed consistently in two or more of the three high-excitation energy data runs (at 165.8, 221.5, and 276.8 MeV) are included. The levels contained in parentheses are more doubtful than the others.

[b]Errors include the uncertainty in the energy of the closest reference peak from the following set: 7.547(3) MeV, 11.080(5) MeV, 15.106(2) MeV.

[c]Full width at half maximum of Breit-Wigner peak shape, corrected for experimental resolution.

TABLE X. Form factors for ^{13}C energy levels above 10 MeV ($\theta=90°$).

	Incident electron energy					
	165.7 MeV		221.3 MeV		276.8 MeV	
E_x MeV	q (fm^{-1})	$F^2\times10^4$	q (fm^{-1})	$F^2\times10^4$	q (fm^{-1})	$F^2\times10^4$
10.753			1.535	0.171(73)	1.925	0.030(28)
10.818	1.142	0.54(12)	1.535	0.145(68)	1.924	0.002(26)
11.080	1.141	5.31(30)	1.534	1.46(11)	1.924	0.213(30)
11.85	1.139	29.3(16)	1.531	29.4(15)	1.921	13.44(70)
12.2	1.138	1.47(26)	1.530	1.04(15)	1.920	0.253(69)
12.4	1.137	2.91(30)	1.530	0.97(13)	1.919	0.332(65)
14.2	1.131	0.15(42)	1.523	0.19(25)	1.913	1.45(11)
14.4	1.130	4.79(53)	1.523	3.32(38)	1.912	0.84(10)
14.6	1.130	4.03(32)	1.522	5.17(34)	1.912	1.89(13)
15.0	1.128	5.77(38)	1.521	3.09(23)	1.910	3.69(24)
15.106	1.128	5.12(28)	1.520	4.55(24)	1.910	2.40(13)
15.5	1.127	1.14(13)	1.519	0.821(90)	1.909	6.18(65)
16.07	1.125	2.25(19)	1.517	3.50(20)	1.907	3.65(20)
16.2	1.124	0.69(14)	1.517	0.289(76)		
18.5			1.509	0.607(85)	1.899	1.25(10)
18.70	1.116	1.63(15)	1.508	3.70(22)	1.898	3.09(18)
20.0	1.112	1.74(17)	1.531	1.77(17)	1.894	1.40(11)
20.4	1.110	1.50(17)	1.503	1.19(12)	1.892	0.71(65)
21.47	1.107	4.90(31)	1.499	13.39(75)	1.889	12.57(66)

prove to be the most difficult to understand theoretically, and further study is needed.

Data have also been taken on states up to 22 MeV excitation energy in ^{12}C. The data on $M4$ transitions to $\frac{7}{2}^+$ and $\frac{9}{2}^+$ states have been published previously.[8] The remaining data, which will be presented in a future publication, mainly concerns lower multipolarity transitions around 14 and 18.7 MeV excitation energy, regions studied by photonuclear and other low-momentum transfer reactions, including electron scattering.[5]

ACKNOWLEDGMENTS

We thank Dr. R. S. Hicks for providing us with unpublished data. This work has been supported by the U.S. Department of Energy under Contract Nos. DE-AC02-76CH00016 and DE-AC02-76ER03069, by the National Science Foundation under Grant No. PHY-8519381, by the Foundation for Fundamental Research on Matter (FOM), and by the Netherlands Organization for Scientific Research (NWO).

TABLE XI. Transverse form factors from 180° measurements.[a]

E_x (MeV)	E_0 (MeV)	q (fm^{-1})	q_{eff} (fm^{-1})	$F_T^2 \times 10^6$
3.68[b]	40	0.385	0.424	148(20)
	45	0.435	0.475	120(9)
	50	0.486	0.525	140(20)
	55	0.536	0.576	118(8)
	60	0.586	0.626	119(12)
	65	0.636	0.676	122(12)
	70	0.687	0.727	110(8)
	80	0.787	0.827	78(7)
	85	0.837	0.877	80(8)
	90	0.887	0.927	66(7)
7.55	45	0.415	0.452	22(7)
	55	0.515	0.554	52(7)
	70	0.666	0.705	75(6)
	80	0.767	0.806	99(7)
	90	0.867	0.906	146(9)
8.86	45	0.407	0.444	33(8)
	55	0.508	0.546	41(7)
	70	0.659	0.698	45(5)
	80	0.760	0.798	35(5)
	90	0.860	0.899	23(7)
9.90[c]	45	0.401	0.438	<6
	55	0.503	0.540	<11
	70	0.654	0.692	<10
10.80[c,d]	70	0.649	0.687	2(4)
	90	0.849	0.888	12(4)
11.80[d]	45	0.390	0.426	34(8)
	55	0.492	0.528	50(7)
	70	0.643	0.681	43(6)
	80	0.744	0.782	33(6)
	90	0.844	0.882	39(6)
14.20[c,d]	55	0.478	0.513	27(7)
	70	0.630	0.667	11(7)
	80	0.731	0.768	24(9)
	90	0.831	0.869	19(8)
15.10[e]	45	0.370	0.404	130(14)
	55	0.473	0.508	131(14)
	70	0.625	0.661	131(15)
	80	0.726	0.763	116(14)
	90	0.826	0.864	122(15)

[a]IKO data.
[b]Sum of 3.68 and 3.85 MeV level (unresolved).
[c]No useful data at incident energies not listed.
[d]May contain some small ^{12}C contributions (abundancy 10% in the target).
[e]^{12}C contribution (also 15.1 MeV) has been subtracted.

APPENDIX A

If harmonic oscillator wave functions are used, we can write the shell-model form factor for any state as

$$F=\left[\frac{2J_f+1}{2J_i+1}\right]^{1/2} Z_0 g^{(0)}+Z_1 g^{(1)} F^{(\lambda\mu)\Delta L\Delta S\Delta J} \quad \text{(A1)}$$

where $Z_{\Delta T}$ denotes the appropriate SU3 OBDME from Table III multiplied by the isospin Clebsch-Gordan coefficient $\langle T_i M_T \Delta T 0 | T_f M_T \rangle$. Also,[42] $g^{(\Delta T)}=\mu^{(\Delta T)}$ if $\Delta S=1$, $g^{(\Delta T)}=F^{(\Delta T)}$ if $\Delta S=0$. For the bare nucleon $\mu^{(0)}=0.88$, $\mu^{(1)}=4.706$, $F^{(0)}=1$, $F^{(1)}=1$. For $\Delta S=1$, the form factors on the right-hand side of Eq. (A1) which we refer to as basic SU3 form factors, can be simply related to the corresponding longitudinal form factors

$$F_T^{\text{el},\Delta J=\Delta L}=\frac{q}{2M}F_L^{\Delta L},$$

$$F_T^{\text{mag},\Delta J=\Delta L+1}=-\frac{q}{2M}\left[\frac{\Delta J+1}{2\Delta J+1}\right]^{1/2} F_L^{\Delta L}, \quad \text{(A2)}$$

$$F_T^{\text{mag},\Delta J=\Delta L-1}=-\frac{q}{2M}\left[\frac{\Delta J}{2\Delta J+1}\right]^{1/2} F_L^{\Delta L},$$

where $q/2M=2(\mu_B/b)y^{1/2}$, $\mu_B=\hbar c/2Mc^2=0.105$ fm.

The basic form factors are given in Table VII.

APPENDIX B

We give the data obtained from our experiments in tabular form.

Table VIII contains the form factors, measured in the CUA-MIT experiment, for electron scattering to the ground state and ten low-lying excited states of ^{13}C.

Table IX presents ^{13}C excitation energies and level widths determined in the CUA-MIT experiments.

Table X contains the 90° form factors for ^{13}C energy levels above 10 MeV excitation energy measured in the CUA-MIT experiment.

Table XI contains the transverse form factors measured in the IKO experiment.

[1]W. Bertozzi, M. V. Hynes, C. P. Sargent, C. Creswell, P. C. Dunn, A. Hirsch, M. Leitch, B. Norum, F. N. Rad, and T. Sasanuma, Nucl. Instrum. Methods **141**, 457 (1977).

[2]G. A. Peterson, Phys. Lett. **25B**, 549 (1967).

[3]G. Wittwer, H.-G. Clerc, and G. A. Beer, Phys. Lett. **30B**, 634 (1969); Z. Phys. **234**, 120 (1970).

[4]C. S. Yang, E. L. Tomusiak, R. K. Gupta, and H. S. Caplan, Nucl. Phys. **A162**, 71 (1971).

[5]J. C. Bergstrom, H. Crannell, F. J. Kline, J. T. O'Brien, J. W. Lightbody, and S. P. Fivozinsky, Phys. Rev. C **4**, 1514 (1971).

[6]F. Ajzenberg-Selove, Nucl. Phys. **A449**, 1 (1986).

[7]R. S. Hicks, private communication.

[8]R. S. Hicks, R. A. Lindgren, M. A. Plum, G. A. Peterson, H. Crannell, D. I. Sober, H. A. Thiessen, and D. J. Millener, Phys. Rev. C **34**, 1161 (1986).

[9]G. J. C. van Niftrik, H. de Vries, L. Lapikás, and C. de Vries, Nucl. Instrum. Methods **93**, 301 (1971).

[10]R. S. Hicks, Nucl. Phys. **A434**, 97c (1985); R. S. Hicks, R. L. Huffman, R. A. Lindgren, G. A. Peterson, M. A. Plum, and J. Button-Shafer, Phys. Rev. C **36**, 485 (1987).

[11]R. S. Hicks, J. Dubach, R. A. Lindgren, B. Parker, and G. A. Peterson, Phys. Rev. C **26**, 339 (1982).

[12]T.-S. H. Lee and D. Kurath, Phys. Rev. C **21**, 293 (1980).

[13]T.-S. H. Lee and D. Kurath, Phys. Rev. C **22**, 1670 (1980).

[14]E. K. Warburton, D. E. Alburger, and D. J. Millener, Phys. Rev. C **22**, 2330 (1980).

[15]S. Cohen and D. Kurath, Nucl. Phys. **73**, 1 (1965).

[16]D. J. Millener and D. Kurath, Nucl. Phys. **A255**, 315 (1975).

[17]S. J. Seestrom-Morris, D. Dehnhard, M. A. Franey, G. S. Kyle, C. L. Morris, R. L. Boudrie, J. Piffaretti, and H. A. Thiessen, Phys. Rev. C **26**, 594 (1982).

[18]D. Dehnhard, S. J. Tripp, M. A. Franey, G. S. Kyle, C. L. Morris, R. L. Boudrie, J. Piffaretti, and H. A. Thiessen, Phys. Rev. Lett. **43**, 1091 (1979).

[19]S. J. Seestrom-Morris, Ph.D. thesis, University of Minnesota, 1981; Los Alamos Report LA-8916-T, 1981.

[20]S. J. Seestrom-Morris, D. Dehnhard, D. B. Holtkamp, and C. L. Morris, Phys. Rev. Lett. **46**, 1447 (1981).

[21]S. J. Seestrom-Morris, M. A. Franey, D. Dehnhard, D. B. Holtkamp, R. L. Boudrie, J. F. Amann, G. C. Idzorek, and C. A. Goulding, Phys. Rev. C **30**, 270 (1984).

[22]S. F. Collins, Ph.D. thesis, University of Melbourne, 1984.

[23]S. F. Collins, G. G. Shute, B. M. Spicer, V. C. Officer, D. W. Devins, D. L. Friesel, and W. P. Jones, Nucl. Phys. **A481**, 494 (1988).

[24]S. F. Collins, G. G. Shute, B. M. Spicer, V. C. Officer, I. Morrison, K. A. Amos, D. W. Devins, D. L. Friesel, and W. P. Jones, Nucl. Phys. **A380**, 445 (1982).

[25]L. Lapikás, G. Box, and H. deVries, Nucl. Phys. **A253**, 324 (1975).

[26]J. C. Bergstrom, private communication.

[27]J. Heisenberg, J. S. McCarthy, and I. Sick, Nucl. Phys. **A131**, 435 (1970).

[28]H. Crannell, Phys. Rev. **148**, 1107 (1966).

[29]L. A. Schaller, L. Schellenberg, T. Q. Phan, G. Piller, A. Ruetschi, and H. Schneuwly, Nucl. Phys. **A379**, 523 (1982).

[30]D. G. Fleming, J. Cerny, C. C. Maples, and N. K. Glendenning, Phys. Rev. **166**, 1012 (1968).

[31]F. Hinterberger, G. Mairle, U. Schmidt-Rohr, P. Turek, and G. J. Wagner, Nucl. Phys. **A106**, 161 (1968).

[32]S. Cohen and D. Kurath, Nucl. Phys. **A101**, 1 (1967).

[33]S. Cohen and D. Kurath, Nucl. Phys. **A141**, 145 (1970).

[34]C. Maples and J. Cerny, Phys. Lett. **38B**, 504 (1972).

[35]D. Kurath and D. J. Millener, Nucl. Phys. **A238**, 269 (1975).

[36]D. J. Millener (unpublished).

[37]J. F. Dubach, Los Alamos Scientific Laboratory Report LA-8303-C, 1980, p. 72.

[38]C. H. Holbow, H. G. Bingham, R. Middleton, and J. D. Garrett, Phys. Rev. C **9**, 902 (1974).

[39]W. D. Teeters and D. Kurath, Nucl. Phys. **A275**, 61 (1977).

[40]H. U. Jäger, H. R. Kissener, and R. A. Eramzhian, Nucl. Phys. **A171**, 16 (1971).
[41]H. D. Knox and R. O. Lane, Nucl. Phys. **A378**, 503 (1982).
[42]T. W. Donnelly and W. C. Haxton, At. Data Nucl. Data Tables **23**, 103 (1979); **25**, 1 (1980).
[43]S. Chakravarti, D. Dehnhard, M. A. Franey, S. J. Seestrom-Morris, D. B. Holtkamp, C. L. Blilie, A. C. Hayes, C. L. Morris, and D. J. Millener, Phys. Rev. C **35**, 2197 (1987).
[44]G. G. Simon, Ch. Schmitt, F. Borkowski, and V. H. Walther, Nucl. Phys. **A333**, 381 (1980).
[45]A. R. Poletti, J. W. Olness, and E. K. Warburton, Phys. Rev. **151**, 812 (1966).
[46]C. L. Blilie, D. Dehnard, M. A. Franey, D. H. Gay, D. B. Holtkamp, S. J. Seestrom-Morris, P. J. Ellis, C. L. Morris, and D. J. Millener, Phys. Rev. C **30**, 1989 (1984).
[47]D. M. Manley, B. L. Berman, W. Bertozzi, T. N. Buti, J. M. Finn, F. W. Hersman, C. E. Hyde-Wright, M. V. Hynes, J. J. Kelly, M. A. Kovash, S. Kowalski, R. W. Lourie, B. Murdock, B. E. Norum, B. Pugh, and C. P. Sargent, Phys. Rev. C **36**, 1700 (1987).
[48]P. W. M. Glaudemans, *Nuclear Shell Models*, edited by M. Vallieres and B. H. Wildenthal (World-Scientific, Singapore, 1985), p. 2.
[49]D. J. Millener, in *Pion-Nucleus Physics: Future Directions and New Facilities at LAMPF*, Proceedings of the Los Alamos Conference on Pion-Nucleus Physics, AIP Conf. No. 163, edited by R. J. Peterson and D. D. Strottman (AIP, New York, 1987).
[50]T. N. Buti, J. Kelly, W. Bertozzi, J. M. Finn, F. W. Hersman, C. Hyde-Wright, M. V. Hynes, M. A. Kovash, S. Kowalski, R. W. Lourie, B. Murdock, B. E. Norum, B. Pugh, C. P. Sargent, and W. Turchinetz, Phys. Rev. C **33**, 755 (1986).
[51]B. E. Norum, M. V. Hynes, H. Miska, W. Bertozzi, J. Kelly, S. Kowalski, F. N. Rad, C. P. Sargent, T. Sasanuma, W. Turchinetz, and B. L. Berman, Phys. Rev. C **25**, 1778 (1982).
[52]V. Horsfjord, Nucl. Phys. **A209**, 493 (1973).
[53]D. J. Millener, J. W. Olness, E. K. Warburton, and S. S. Hanna, Phys. Rev. C **28**, 497 (1983).
[54]J. M. Bang, F. G. Gareev, W. T. Pinkston, and J. S. Vaagen, Phys. Rep. **125**, 253 (1985).
[55]J. Heisenberg and H. P Blok, Annu. Rev. Nucl. Sci. **33**, 569 (1983).
[56]C. D. Goodman, R. C. Byrd, I. J. Van Heerden, T. A. Cary, D. J. Horen, J. S. Larsen, C. Gaarde, J. Rapaport, T. P. Welch, E. Sugarbaker, and T. N. Taddeucci, Phys. Rev. Lett. **54**, 877 (1985); **54**, 2060(E) (1985).
[57]N. S. P. King, P. W. Lisowski, G. L. Morgan, P. N. Craig, R. G. Jeppesen, D. A. Lind, J. R. Shepard, J. L. Ullman, C. D. Zafiratos, C. D. Goodman, and C. A. Goulding, Phys. Lett. B **175**, 279 (1986).
[58]I. S. Towner and F. C. Khanna, Nucl. Phys. **A399**, 334 (1983).
[59]T. Sato, K. Koshigiri, and H. Ohtsuko, Z. Phys. A **320**, 507 (1985).
[60]H. Ohnuma, N. Hoshino, O. Mikoshiba, K. Raywood, A. Sakaguchi, G. G. Shute, B. M. Spicer, M. H. Tanaka, M. Tanifuji, T. Teresawa, and M. Yasue, Nucl. Phys. **A448**, 205 (1985).
[61]R. J. Holt, R. M. Laszewski, H. E. Jackson, J. E. Monahan, and J. R. Specht, Phys. Rev. C **21**, 1699 (1980).
[62]B. A. Brown and B. H. Wildenthal, Nucl. Phys. **A474**, 290 (1987).
[63]B. A. Brown and B. H. Wildenthal, At. Data Nucl. Data Tables **33**, 347 (1985).
[64]A. G. M. van Hees, A. A. Wolters, and P. W. M. Glaudemans, Nucl. Phys. **A476**, 61 (1988).